Atmospheric Deposition of Reactive Nitrogen to a Deciduous Forest in the Southern Appalachian Mountains

John T. Walker[1], Xi Chen[1a], Zhiyong Wu[1b], Donna Schwede[1], Ryan Daly[1c], Aleksandra Djurkovic[1], A. Christopher Oishi[2], Eric Edgerton[3], Jesse Bash[1], Jennifer Knoepp[2§], Melissa Puchalski[4], John Iiames[1], Chelcy F. Miniat[2d]

[1]*U.S. Environmental Protection Agency, Office of Research and Development, Durham, NC, USA*
[2]*U.S. Department of Agriculture, Forest Service, Otto, NC, USA*
[3]*Atmospheric Research and Analysis, Inc., Cary, NC, USA*
[4]*U.S. Environmental Protection Agency, Office of Air and Radiation, Washington, DC, USA*
[a]*Now at: U.S. Environmental Protection Agency, Office of Air Quality Planning and Standards, Durham, NC, USA*
[b]*Now at: RTI International, Durham, NC, USA*
[c]*Now at: Boulder A.I.R. LLC, Boulder, CO, USA*
[d]*Now at: U.S. Department of Agriculture, Forest Service, Albuquerque, NM, USA*
[§]*Recently retired*
Correspondence to: John T. Walker (walker.johnt@epa.gov)

Abstract. Assessing nutrient critical load exceedances requires complete and accurate atmospheric deposition budgets for reactive nitrogen (N_r). The exceedance is the total amount of N_r deposited to the ecosystem in excess of the critical load, which is the amount of N_r input below which harmful effects do not occur. Total deposition includes all forms of N_r (i.e., organic and inorganic) deposited to the ecosystem by wet and dry pathways. Here we present results from the Southern Appalachian Nitrogen Deposition Study (SANDS), in which a combination of measurements and field-scale modeling were used to develop a complete annual N_r deposition budget for a deciduous forest at the Coweeta Hydrologic Laboratory. Wet deposition of ammonium, nitrate, nitrite, and bulk organic N were measured directly. The dry deposited N_r fraction was estimated using a bidirectional resistance-based model driven with speciated measurements of N_r air concentrations (e.g., ammonia, ammonium aerosol, nitric acid, nitrate aerosol, bulk organic N in aerosol, total alkyl nitrates, and total peroxy nitrates), micrometeorology, canopy structure, and biogeochemistry. Total annual deposition was $\sim$ 6.7 kg N ha^{-1} yr^{-1}, which is on the upper end of N_r critical load estimates recently developed for similar ecosystems in nearby Great Smoky Mountains National Park. Of the total (wet + dry) budget, 51.2% was contributed by reduced forms of N_r (NH_x = ammonia + ammonium), with oxidized and organic forms contributing $\sim$ 41.2% and 7.6%, respectively. Our results indicate that reductions in NH_x deposition would be needed to achieve the lowest estimates ($\sim$ 3.0 kg N ha^{-1} yr^{-1}) of N_r critical loads in southern Appalachian forests.

1 Introduction

35   Prior to the Industrial Revolution, Earth's ecosystems received reactive nitrogen (N_r) deposition rates of ~0.5 kg ha^{-1}

36   yr^{-1} (Holland et al., 1999). Since the 19th century, anthropogenic activities, both industrial and agricultural, have

37   resulted in unprecedented quantities of N_r being released into the atmosphere, subsequently altering biogeochemical

38   cycles (Neff et al., 2002a,b; Ollinger et al., 2002; Bragazza et al., 2006; Doney et al., 2007; Galloway et al., 2008;

39   Boonstra et al., 2017). Excessive atmospheric deposition of N_r to terrestrial ecosystems may lead to soil and aquatic

40   acidification, nutrient imbalance and enrichment, plant damage and microbial community changes as well as loss of

41   biodiversity (Bobbink et al., 1998; Lohse et al., 2008; Simkin et al., 2016). Nitrogen deposition rates in many areas,

42   including North America, Europe and Asia, exceed 10 kg ha^{-1} yr^{-1} and may double current rates by the year 2050 in

43   some regions (Galloway et al., 2008).

44   The amount of N_r deposition below which significant harmful effects do not occur is known as the critical load

45   (Nilsson and Grennfelt, 1988). Critical loads can be quantified using empirical relationships between ecosystem N

46   input and ecosystem response (Pardo et al., 2011; Root et al., 2015), or mass balance type biogeochemical models

47   (Lynch et al., 2017; McNulty et al., 2007). For the southern Appalachian Mountains, simple mass balance approaches

48   yield critical loads similar to those derived from empirical approaches for forest health and biogeochemical responses.

49   In a recent study employing a mass balance model for the Great Smoky Mountains National Park, Pardo et al. (2018)

50   quantified critical loads for spruce-fir, beech, and mixed deciduous forests in the range of 2.8 to 7 kg N ha^{-1} yr^{-1}, with

51   the highest value corresponding to a high-elevation spruce-fir site experiencing disturbance-induced regrowth.

52   Accurate and complete deposition budgets (i.e., including all forms of N) are required to quantify the amount of N

53   input to ecosystems in excess of the critical load (i.e., the critical load exceedance).

54   Estimates of N deposition for critical load assessments can be derived from gridded chemical transport models (CTMs)

55   (Ellis et al., 2013; Lee et al., 2016; Simkin et al., 2016; Clark et al., 2018; Makar et al., 2018), measurement-model

56   fusion (MMF) techniques that combine measurements with CTM output (Schwede and Lear, 2014; Nanus et al., 2017;

57   McDonnell et al., 2018; U.S. EPA, 2019a), or inferential modeling with site specific measurements (Flechard et al.,

58   2011; Li et al., 2016). While these approaches reflect the state-of-the-science and are widely used, they collectively

59   suffer from incompleteness of the N deposition budget (and are therefore biased low) (Walker et al., 2019a).

60   Monitoring networks for wet deposition (NADP/NTN) and air concentrations of N_r (CASTNET) focus only on

61   inorganic species, excluding organic forms of N which account for ~ 25% of total N in wet deposition on average

62   (Jickels et al., 2013). Due to difficulties in sampling (Walker et al., 2012) and the inability to fully speciate the wide

63   range of constituents (Neff et al., 2002a; Altieri et al., 2009, 2012; Cape et al., 2011; Samy et al., 2013, Chen et al.,

64   2018), organic N is not routinely monitored. Hence, deposition of organic N remains uncertain, and thus N deposition

65   budgets developed from network monitoring data and CTMs remain incomplete.

66   Current N deposition estimates also have a relatively high degree of uncertainty in the estimation of dry deposition.

67   While wet deposition is routinely measured, direct measurements of dry N_r deposition (i.e., flux measurements) in

68   North America are relatively few (Walker et al., 2020). Estimates of dry deposition for ecosystem assessments are

69   therefore derived from models (Schwede and Lear, 2014; Li et al., 2016; Lee et al., 2016). Of the inorganic N species,

70 NH$_3$ is the most important contributor to dry deposition in many areas (Walker et al., 2019b) but also the most

71 uncertain (Flechard et al., 2011) due to the bi-directionality of surface-atmosphere exchange. A paucity of flux

72 measurements (Walker et al., 2020) precludes bias correction of dry deposition in CTMs and MMF techniques, making

73 dry deposition much more uncertain relative to wet deposition.

74 The Coweeta study site represents southern Appalachian Mountain forests, highly diverse and productive ecosystems

75 that provide a variety of ecosystem services, including a source of surface drinking water (Caldwell et al., 2014).

76 While deposition of oxidized N to forests in the southeastern U.S. has declined in response to the Clean Air Act,

77 montane ecosystems continue to receive high rates of deposition due to elevation-induced precipitation gradients

78 (Weathers et al., 2006; Knoepp et al., 2008). Southern Appalachian forests continue to show signs of sensitivity to N

79 deposition. For example, litterfall N fluxes and foliar N concentrations at Coweeta have steadily increased over the

80 past two decades (Knoepp et al., 2018). Highly spatially variable meteorological patterns typical of complex terrain

81 are difficult to model (Lehner and Rotach, 2018), leading to uncertainties in precipitation amounts and wet deposition

82 (Zhang et al., 2018) as well as the micrometeorological processes that govern dry deposition (Cowan et al., 2022).

83 Estimates of deposition from gridded CTMs in mountainous terrain therefore contain a higher degree of uncertainty

84 relative to low-elevation ecosystems. For these reasons, a better understanding of total N deposition in southern

85 Appalachian forests is needed.

86 This study investigates the N deposition budget in a remote montane forest in the southeastern U.S. We combine long-

87 term (1978 – 2020) and seasonal intensive (2015-2016) measurements of wet deposition, speciated air concentrations

88 of N$_r$, micrometeorology, biogeochemistry and forest canopy structure with in-situ inferential dry deposition modeling

89 to develop an annual, speciated, total N deposition budget, including net and component NH$_3$ fluxes as well as dry

90 and wet organic N deposition. Seasonal and annual total N deposition fluxes are presented in the context of long-term

91 trends in air concentrations and wet deposition of inorganic N species. Spatial representativeness is characterized

92 using measurements of air concentrations of the primary inorganic N species and previous wet deposition

93 measurements along an elevation gradient across the topographically complex forested basin.

2 Methods

2.1 Site description

95 The study was conducted at the USDA Forest Service Coweeta Hydrologic Laboratory, a 2,185-ha experimental forest

96 in southwestern North Carolina, USA (35°3' N, 83°25' W) near the southern end of the Appalachian Mountain

97 chain. Topography is complex, with elevations ranging from 675 to 1592 m within the Coweeta Basin. Mean annual

98 temperature and precipitation are 12.9 °C and 1795 mm, respectively. Dominant overstory species are *Liriodendron*

99 *tulipifera*, *Quercus alba*, *Betula lenta*, and *Acer rubrum*, which comprise 24%, 17%, 11%, and 8% of the basal area,

100 respectively, in the low-elevation forests where the study was conducted (Oishi et al., 2018). The dominant understory

101 woody shrub species is *Rhododendron maximum* (evergreen), which comprises 13% of the basal area (Oishi et al.,

102 2018). Species composition in the vicinity of the eddy flux tower (EFT), further described below, is detailed in Table

103 S1. Canopy height surrounding the EFT is ~ 30 m.

104   The Coweeta Basin has been a long-term monitoring site for atmospheric chemistry and deposition since the late
105   1970s. Weekly wet deposition of ammonium (NH_4^+) and nitrate (NO_3^-), along with sulfate (SO_4^{2-}), chloride, and base
106   cations have been measured as part of the NADP/NTN (Site NC25, https://nadp.slh.wisc.edu/networks/national-
107   trends-network/) since 1978. Weekly integrated air concentrations of particulate NH_4^+, NO_3^-, SO_4^{2-}, chloride, and base
108   cations, as well as nitric acid (HNO_3) and sulfur dioxide (SO_2), have been measured by CASTNET (Site COW137,
109   https://www.epa.gov/castnet) since 1987. Since 2011, biweekly integrated air concentrations of ammonia (NH_3) have
110   been   measured   by   the   NADP   Ammonia   Monitoring   Network   (AMoN   Site   NC25,
111   https://nadp.slh.wisc.edu/networks/ammonia-monitoring-network/). Here we use these datasets to place our study
112   results into historical context, supplement the more intensive atmospheric chemistry measurements described below,
113   and as inputs for inferential modeling of dry deposition. The long-term NADP and CASTNET measurements are
114   collected in the lower part of the basin, indicated as NC25/COW137 in Figure 1.

115   **2.2 Southern Appalachian Nitrogen Deposition Study**

116   Building on the long-term NADP and CASTNET measurements described above, the Southern Appalachian Nitrogen
117   Deposition Study (SANDS) was conducted in 2015 and 2016 to better understand the atmospheric chemistry and
118   deposition of reactive nitrogen at Coweeta. Intensive measurement campaigns were conducted from May 21–June 9,
119   2015; August 6–25, 2015; September 9–26, 2015; April 19–May 11, 2016; and July 13–August 3, 2016. A subset of
120   measurements was conducted continuously between May 2015 to August 2016. As described below, time-resolved
121   and time-integrated measurement techniques were used to characterize organic N in the gas phase, in particulate
122   matter, and in wet deposition; the temporal variability of air concentrations of gas-phase oxidized and reduced forms
123   of N; and the spatial variability of atmospheric N concentrations across the Coweeta Basin. Vertical profiles of air
124   concentrations were measured within the forest canopy to examine source/sink processes and measurements of soil
125   and vegetation chemistry were conducted to characterize NH_3 emission potentials. Measurements were combined with
126   NADP and CASTNET data to develop seasonal and annual total N deposition budgets employing inferential modeling
127   for the dry deposition component. Vertical concentration profile and biogeochemical measurements were used to
128   inform the parameterization of NH_3 bi-directional exchange. Sampling locations are described in Figure 1 and Table
129   1. Measurement details are summarized in Table 2.

130   **2.2.1 Wet deposition**

131   Additional wet deposition measurements were conducted adjacent to the NTN NC25 sampler to quantify the
132   contribution of bulk water-soluble organic N (WSON) to water-soluble total nitrogen (WSTN) in precipitation.
133   Weekly precipitation samples were collected in a modified wet-only sampler with a borosilicate glass funnel and
134   amber glass bottle (Walker et al., 2012), shielded from sunlight, and maintained in the field under continuous
135   refrigeration to maintain the stability of ON until retrieval (Walker et al., 2012). Samples were sent to the NADP
136   Central Analytical Laboratory on ice for analysis of NH_4^+, NO_3^-, NO_2^-, and WSTN as described by Walker et al.
137   (2012).   WSON   concentration   was   calculated   as:
138    $WSON = WSTN - (NH_4^+ + NO_3^- + NO_2^-)$ (1)

139 The method detection limit for WSON is 10 µg N L^{-1} (Walker et al., 2012). These measurements were collected
140 continuously from February 2015 to August 2016.

141 During the spring of 2015, thymol was added to the precipitation collection bottle as a biocide to inhibit organic
142 nitrogen loss in the sample should the refrigerated collector malfunction or lose power. Thymol negatively affected
143 the precision of the total nitrogen measurement, and its use was discontinued in fall of 2015. Ultimately, there were
144 no issues with the refrigerated collector, and the thymol-containing samples were excluded from the analysis presented
145 herein. However, this data loss resulted in a gap from August 2015 to mid-October 2015 of the 12-month period for
146 which the total deposition budget is developed. The data gap comprised eight weekly periods in which precipitation
147 occurred. For this period, the NH_4^+ and NO_3^- concentrations from the collocated NADP/NTN NC25 sampler were
148 used. Based on the SANDS measurements, the ON concentration during this period was estimated by assuming that
149 $NH_4^+ + NO_3^-$ contribute 89% of total nitrogen in rainfall, with WSON representing the balance (11%). For the annual
150 budget, weekly concentrations were combined with measured precipitation depth to calculate weekly deposition (kg
151 N ha^{-1}). Comparison between SANDS and NTN concentrations of NH_4^+ and NO_3^- showed very good agreement
152 (Supplemental Section S1, Figure S1).

153 2.2.2 Air concentrations

154 Hourly concentrations of NOy, HNO_3, total gas-phase peroxy nitrates (ΣPN), and total gas-phase alkyl nitrates (ΣAN)
155 were measured continuously from August 2015 to August 2016 at the height of 8 m adjacent to the COW137
156 CASTNET tower (Figure 1, Tables 1 and 2). NOy and HNO_3 were measured using a modified model 42S NO-NO$_2$-
157 NOx analyzer; the NOy technique is described in detail by Williams et al. (1998). Briefly, total oxidized reactive
158 nitrogen (NOy) is converted to NO using a molybdenum catalyst heated to 325 ºC. On a second channel, a metal
159 denuder coated with potassium chloride (KCl) is used to remove HNO_3 before passing through a second molybdenum
160 converter heated to 325 ºC. The difference between the total NOy measurement and the HNO_3-scrubbed NOy
161 measurement is interpreted as HNO_3. Here we refer to the method as denuder difference chemiluminescence (DD-
162 CL).

163 Total peroxynitrates (ΣPNs) and total alkylnitrates (ΣANs) were measured using a modification of the technique
164 described by Day et al. (2002), in which PNs and ANs are thermally decomposed to NO_2 followed by measurement
165 of the incremental NO_2 above ambient background for each decomposition step. Day et al. (2002) quantified NO_2 via
166 laser induced fluorescence, while photolytic conversion to NO and quantification of the resulting NO by NO-O$_3$
167 chemiluminescence is used in the current study. Here we refer to the method as thermal decomposition, photolytic
168 conversion, chemiluminescence (TD-PC-CL). A single chemiluminescence analyzer was used for NOy, HNO_3, ΣPN,
169 and ΣAN measurements. Additional detail on the instrument and associated QA/QC procedures is included in
170 Supplemental Section S2.

171 Hourly concentrations of NH_3 and HNO_3 were measured on the eddy flux tower (EFT, Figure 1, Tables 1 and 2) at
172 two heights above the canopy (34 m and 37.5 m above ground during spring, 2016; 34 m and 43.5 m above ground
173 during summer, 2016) using the Monitor for Aerosols and Gases in Ambient Air (MARGA, Metrohm Applikon B.V.,
174 the Netherlands). Details and principles of the MARGA system have been previously described (Rumsey and Walker,

175   2016; Chen et al., 2017). Briefly, the MARGA 2S consisted of two sampler boxes positioned on the tower and a

176   detector box located in a climate-controlled enclosure at the base of the tower. Sample boxes comprised an inlet of

177   1.27 cm outer diameter 30 cm long PFA Teflon tubing with no particle size selection, through which air flow was

178   mass controlled at ~ 16.7 L min^{-1}, a wet rotating denuder (WRD) for collection of soluble gases, and a steam jet aerosol

179   collector (SJAC). Liquid sample from the WRD and SJAC is continuously drawn from the sample boxes down the

180   tower to the analytical box for analysis by Ion Chromatography (IC) on an hourly basis at the detector unit located in

181   a climate-controlled enclosure at the base of the tower. At the beginning and end of the measurement intensive, multi-

182   level liquid NO_3^- and NH_4^+ standards were introduced at the WRD and SJAC, with airflow turned off, to assess the

183   analytical accuracy of the NH_3 and HNO_3 measurement. MARGA measurements were conducted during the spring

184   and summer of 2016 intensives. Comparisons of continuous and time-integrated methods for HNO_3 and NH_3 are

185   summarized in Supplemental Section S1 (Figures S2 and S3).

186   Concentrations of NH_3, HNO_3, SO_2, NH_4^+, NO_3^-, and SO_4^{2-} in air were measured concurrently on the EFT at 10 heights

187   from just above the forest floor (0.5 m above ground) to several meters above the canopy (upper height of 37 m above

188   ground during spring 2016, 43.5 m above ground during summer, 2016) using a glass annular denuder/filter pack

189   (URG Corporation, Chapel Hill, NC) system. The sampling assembly included a 1% Na_2CO_3 coated denuder for

190   collection of acid gases followed by a 1% H_3PO_3 coated denuder for collection of NH_3, and a filter pack containing a

191   primary Teflon filter for collection of aerosol and a backup Nylon filter (47 mm, Pall Corp, Port Washington, NY) to

192   collect HNO_3 liberated by dissociation of NH_4NO_3 on the primary filter. Inlets were Teflon coated glass impactors

193   with a nominal 2.5 μm aerodynamic diameter cutpoint (URG Corporation, Chapel Hill, NC). Sample durations were

194   typically 3 or 4 h at a flow rate of ~ 16.7 L min^{-1}. Flow rates were controlled by critical orifice and were verified

195   before and after each sampling period with a NIST traceable primary standard flow meter (Bios DryCal DC-Lite

196   flowmeter, Mesa Laboratories, Inc., Lakewood, CO).

197   Denuders and filters were extracted with 10 mL of deionized water and analyzed by ion chromatography (IC, Dionex

198   model ICS-2100, Thermo Scientific, Waltham, MA). Extracts were analyzed for cations using Dionex IonPac 2-mm

199   CG12 guard and CS12 analytical columns; separations were conducted using 20 mM methanesulfonic acid (MSA) as

200   eluent at a flow rate of 0.25 mL min^{-1}. Anions were analyzed (IonPac 2-mm AG23 guard column, AS23 analytical

201   columns) using an isocratic eluent mix of carbonate/bicarbonate (4.5/0.8mM) at a flow rate of 0.25 mL min^{-1}. Multi-

202   point (≥5) calibrations were conducted using a mixture prepared from individual inorganic standards (Inorganic

203   Ventures, Christiansburg, VA). A mid-level accuracy check standard was prepared from certified standards mix

204   (AccuStandard, New Haven, CT) for quality assurance/quality control. Profile measurements were conducted during

205   each of the five SANDS intensives.

206   Bulk organic nitrogen in aerosols was measured using a high-volume (Hi-Vol) Tisch TE-1000 (Tisch Environmental,

207   Cleves, OH) dual cyclone $PM_{2.5}$ sampler operated at a flow rate of 230 L min^{-1}. The unit was deployed at ground level

208   adjacent to the COW137 CASTNET tower and collected 24 h (started at 7 A.M. local time) integrated samples on

209   pre-baked (550 °C for 12 h) quartz fiber (QF) filters (90-mm, Pall Corp, Port Washington, NY). Field blanks were

210   collected the same way except being loaded in the sampler without the pump switched on. A QF punch (1.5 cm^2) from

211   each sample was extracted with DI water (18.2 MΩ·cm, Milli-Q Reference system, Millipore, Burlington, MA) in an

212   ultrasonic bath for 45 min. The sample extract was filtered through a 0.2-µm pore size PTFE membrane syringe filter

213   (Iso-disc, Sigma Aldrich, St. Louis, MO) before subsequent analyses.

214   Water-soluble total N (WSTN) concentrations were measured using a high-temperature catalytic combustion and

215   chemiluminescence method that included a total organic carbon analyzer (TOC-VCSH) combined with a total nitrogen

216   module (TNM-1) (Shimadzu Scientific Instruments, Columbia, MD). Briefly, the TN module converts all nitrogen

217   compounds to NO at 720 ℃ in a combustion chamber, and NO is quantified by NO_2 chemiluminescence through

218   reaction with ozone. A 5-point calibration was conducted with KNO_3 standard solution for each batch of samples.

219   Before and after each batch of samples being analyzed, a suite of quality assurance check analysis including lab DI

220   and accuracy check standard were conducted to ensure accuracy and precision. Inorganic species (NH_4^+, NO_3^-, NO_2^-)

221   were analyzed by IC as described above, and WSON was calculated according to equation (1). Comparisons of Hi-

222   Vol and CASTNET PM measurements are summarized in Supplemental Section S1 (Figure S4).

223   To evaluate the spatial distribution of gaseous N across the Coweeta Basin, additional passive sampling of HNO_3 and

224   NH_3 was conducted across an elevation gradient for the full year of 2015 (Figure 1, Tables 1 and 2). Samplers were

225   deployed for two-week periods at the height of 10 m above ground on an aluminum tilt-down tower. NH_3

226   measurements followed AMoN methods. HNO_3 was collected on 47-mm Nylon filters (Nylasorb, Pall Corp, Port

227   Washington, NY) as described by Bytnerowicz et al. (2005). NH_3 and HNO_3 sampler preparation and analysis was

228   performed by the NADP Central Analytical Laboratory and CASTNET laboratories, respectively. Field calibration of

229   the passive HNO_3 measurements (Supplemental Figure S5) was based on comparison with a collocated CASTNET

230   sampler at Screwdriver Knob site (Figure 1, Tables 1 and 2), which also operated for the full year of 2015.

231   **2.2.3 Micrometeorology**

232   Site characteristics of micrometeorology and ecosystem fluxes of water and carbon dioxide have been previously

233   described (Novick et al., 2013; 2014; Oishi et al., 2018). Three-dimensional wind components were measured by sonic

234   anemometer (Model 81000, R.M. Young Company, Traverse City, MI) above the forest canopy on the EFT.

235   Momentum and kinematic heat fluxes were determined by eddy covariance (EC) from sonic data. For EC calculations,

236   raw 10-Hz sonic data were processed into hourly averages after block average detrending and 2D coordinate rotation

237   (Novick et al., 2013). Air temperature and relative humidity (RH) were measured at the top of the tower (EC155,

238   Campbell Scientific, Logan, UT) and 2/3 canopy height (HMP-45, Vaisala, Helsinki, Finland). Photosynthetically

239   active radiation (PAR; LI-190, LI-COR Biosciences, Lincoln, NE) and upward and downward, shortwave and

240   longwave radiation (CNR 4, Kipp & Zonen, Delft, The Netherlands) were measured at the top of the tower. Surface

241   wetness was measured in the canopy crown, understory and at the ground using leaf wetness sensors (Model 237,

242   Campbell Scientific). Soil volumetric water content (VWC) averaged over 0–30 cm depth was measured in four

243   locations around the tower using time domain reflectometry probes (CS616, Campbell Scientific). Soil temperture

244   was measured at four depths (5, 20, 35, and 55 cm) in two locations near the tower using thermistors. For missing

245   data, linear interpolation was used to fill short gaps (1–4 h). Longer gaps were filled by substitution using the average

246   hourly diel profile calculated for each month. Micrometeorological data were used for inferential dry deposition

247   modeling as described below.

2.2.4 Biogeochemistry

Ammonia emission potentials (Γ) and compensation points for live vegetation, leaf litter on the forest floor, and soil were estimated from measurements of NH_4^+ and pH in the leaf and litter tissue and soil pore water (Massad et al., 2010). Green leaves were collected from 18 species (Table S1) within the flux footprint of the tower and other locations in the Coweeta Basin. Leaf litter was collected along transects extending to the northeast and southwest (i.e., predominant wind directions) of the flux tower ~100 m. Litter included a composite of intact leaves and leaf fragments and excluded the more decomposed material at the top of the organic soil layer. Approximately 5 g of leaf tissue was ground in liquid nitrogen using a mortar and pestle and small coffee grinder, then extracted with 20 mL of deionized water. pH was determined directly on the extracts (Oakton pH 2100 meter, Mettler Toledo InLab Micro electrode). The $[NH_4^+]$ in the extracts, which reflects the bulk tissue concentration, was determined by ion chromatography as described above for denuder measurements either directly or, for samples with high organic content, after separation of the NH_4^+ from the solution as NH_3 using headspace equilibration. For the headspace method, 5 mL of tissue extract was added to a 250-mL high-density polyethylene jar containing two ALPHA passive samplers (Center for Ecology and Hydrology; Tang et al., 2001), without the diffusion barrier, affixed to the interior of the lid. The jar was sealed, and 5 mL of 0.3 N NaOH was added to the extract via a septum. The NH_3 liberated from the liquid extract into the headspace was collected by the passive diffusion samplers over a period of 48 h, after which the passive sampler was extracted with 10 mL of deionized water. Extracts were then analyzed by ion chromatography as described above.

Emission potentials of the vegetation (Γ_s) and litter (Γ_l) were estimated from measured concentrations of $[H^+]$ (M) and $[NH_4^+]$ (μg g^{-1} tissue fresh weight) in the bulk tissue as:

$$\Gamma_{s,l} = \frac{[NH_4^+] \times (5.56E^{-5}) \times LD}{[H^+]} \tag{2}$$

where LD is leaf density (kg L^{-1} fresh tissue, equivalent to g cm^{-3} fresh tissue). In this case, LD for woody deciduous and woody evergreen species are 0.37 and 0.42 kg L^{-1}, respectively (Poorter et al., 2009). Emission potentials for litter, which consisted of a mix of in-tact or partial leaves and needles, assume an average density of 0.4 kg L^{-1}. The factor of $5.56E^-5$ in equation 2 is necessary to convert $[NH_4^+]$ from μg NH_4^+ g^{-1} tissue to mol NH_4^+ kg^{-1} tissue.

Soil chemistry was measured in 20 m x 20 m plots located in the vicinity of the tower. During 2010, soil NH_4^+ was determined on soil samples collected with PVC cores (5-cm diameter and 10-cm deep) in four locations (replicates) within each of four plots. Samples were collected bi-monthly during the growing season. NH_4^+ was extracted within two hours of collection using 5 g of sieved (<5 mm) soil in 20 mL of 2M potassium chloride followed by colorimetric analysis (Astoria2 autoanalyzer, Astoria-Pacific International; Coweeta Hydrologic Laboratory, 2016). Soil pH was measured on 0–10 cm samples collected in three plots in winter of 2013 (each sample representing a composite of 20–25 2.5-cm diameter soil cores). Soil pH was determined directly after mixing 5 g soil with 10 mL 0.01M calcium chloride (Coweeta Hydrologic Laboratory, 2016). Soil emission potential (Γ_{soil}) (unitless) was estimated directly from measured molar concentrations of $[H^+]$ and $[NH_4^+]$ as:

$$\Gamma_{soil} = \frac{[NH_4^+]}{[H^+]} \tag{3}$$

2.2.5 Above-canopy flux measurements

Above-canopy fluxes of NH_3 and HNO_3 were quantified from measurements of vertical concentration gradients conducted during the final (summer 2016) intensive when the tower was at maximum height and the greatest vertical separation of concentration measurements was achieved. Fluxes were determined using the modified Bowen-ratio (MBR) method (Meyers et al., 1996) as:

$$F = -K_c(z)\frac{dC}{dz} \,, \tag{4}$$

where K_c and dC/dz are the eddy diffusivity and vertical concentration gradient of the chemical species of interest. The value of K_c for trace gases was assumed equivalent to the eddy diffusivity of heat (K_t), calculated as:

$$K_c = K_t = -\overline{w't'}\frac{\Delta z}{\Delta t} \,, \tag{5}$$

where $\overline{w't'}$ is the kinematic surface heat flux measured by eddy covariance above the canopy (43.5 m above ground level), Δt is the air temperature difference between the levels at 43 m and 35 m above ground level, and Δz is the height interval of air temperature measurements. Air temperature was measured using aspirated thermocouples, and Δt was corrected for a small bias between the sensors determined by collocated comparison. Concentration gradients were determined from URG annular denuder measurements at 34.6 m and 43 m above ground level, as described above in section 2.2.2. Given the complexity of the topography, no attempt was made to correct for potential roughness sub-layer effects on either the eddy diffusivity or concentration gradients, which should be acknowledged as a source of uncertainty in the calculated HNO_3 and NH_3 fluxes. Additional detail on the gradient measurements is included in Supplemental Section S3.

2.2.6 Seasonal and annual deposition budget

Speciated seasonal and annual total nitrogen deposition budgets were developed for the period August 2015 to August 2016. The wet deposited components, including NH_4^+, NO_3^-, and total WSON, were directly measured. Speciated dry deposition was estimated by combining measured air concentrations, micrometeorology, biogeochemistry and canopy physical characteristics within a box version of the Surface Tiled Aerosol and Gaseous Exchange (STAGE) model, which is an option in the Community Multi-scale Air Quality Model (CMAQ) version 5.3 (Appel et al., 2021). The STAGE model treats the deposition of gases and particles separately. The air-surface exchange of gases is parameterized as a gradient process and is used for both bidirectional exchange and dry deposition following the widely used resistance model of Nemitz et al. (2001) and Massad et al. (2010):

$$F = -f_{veg}\frac{\chi_a(z)-\chi_{z_0}}{R_a} - \left(1-f_{veg}\right)\frac{\chi_a(z)-\chi_g}{R_a+R_g} \,, \tag{6}$$

where F is the net flux above the canopy (a negative value represents a net deposition flux and a positive value represents a net emission flux), which is the sum of the component cuticular (F_{cut}), stomatal (F_s), and ground (F_g) fluxes. The quantity $\chi_a(z)$ is the ambient concentration at a reference height (z), χ_{z_0} is the concentration at height d (displacement height) + z_0 (roughness length), χ_g is the ground layer compensation point, R_a is the aerodynamic resistance between z and $d + z_0$, R_g is the total ground resistance including in-canopy aerodynamic resistance (R_{inc}),

315 ground boundary layer resistance (R_{bg}), and soil resistance (R_{soil}) ($R_g = R_{inc} + R_{bg} + R_{soil}$), and f_{veg} is the vegetation

316 coverage fraction. The ground is fully covered by vegetation at our forested site, and f_{veg} is therefore set to 1.

317 The quantity χ_{z0} is related to the canopy (χ_c) and ground compensation points (χ_g) according to:

318
$$\chi_{z_0} = \frac{\left(\frac{\chi_a(z)}{R_a} + \frac{\chi_c}{R_{bl}} + \frac{\chi_g}{R_g}\right)}{\left(\frac{1}{R_a} + \frac{1}{R_{bl}} + \frac{1}{R_g}\right)} , \tag{7}$$

319 where R_{bl} is the leaf boundary layer resistance. χ_c follows Nemitz et al. (2001) but is modified to account for a cuticular

320 compensation point (χ_{cut}):

321

$$\chi_c = \frac{\chi_a(z)(R_a R_{bl})^{-1} + \chi_s\left[(R_a R_s)^{-1} + (R_{bl} R_s)^{-1} + (R_g R_s)^{-1}\right] + \chi_{cut}\left[(R_a R_{cut})^{-1} + (R_{bl} R_{cut})^{-1} + (R_g R_{cut})^{-1}\right] + \chi_g\left(R_{bl} R_g\right)^{-1}}{(R_a R_{bl})^{-1} + (R_a R_s)^{-1} + (R_a R_{cut})^{-1} + (R_{bl} R_g)^{-1} + (R_{bl} R_s)^{-1} + (R_{bl} R_{cut})^{-1} + (R_g R_s)^{-1} + (R_g R_{cut})^{-1}} , \tag{8}$$

322
323
324

325 where χ_s is the leaf stomatal compensation point, and R_s and R_{cut} are the stomatal and cuticular resistances, respectively.

326 The stomatal, cuticular, and ground compensation points ($\chi_s, \chi_{cut}, \chi_g$) are described according to Nemitz et al. (2000a)

327 as a function of temperature (T) and the emission potentials (Γ):

328
$$\chi_{s,cut,g} = \frac{161512}{T} 10^{\frac{-4507.11}{T}} \Gamma_{s,cut,g} . \tag{9}$$

329 Γ_{cut} is set to 0 in this study, and thus, there is only deposition to leaf cuticles. For unidirectional exchange of gases

330 other than NH_3, Γ_s and Γ_g are also set to 0. In the case of NH_3, the foliage and ground layers may act as a source or

331 sink depending on the ratio of the ambient concentration to the respective compartment compensation point (Husted

332 and Schjoerring, 1995). Here values of Γ for NH_3 are derived from measurements of live vegetation, litter, and soil

333 chemistry as described above. Values used in the base model simulation are described in Section 3.6, and the

334 sensitivity of modeled NH_3 fluxes to Γ is discussed in Supplemental Section S5.

335 Formulas for each resistance component are summarized in Supplemental Table S2. The resistances are largely

336 estimated following Massad et al. (2010) with the following exceptions. The value of R_s is based on the Noah (Chen

337 and Dudhia, 2001) or P-X land surface schemes (Pleim and Xiu, 1995) in the Weather Research and Forecasting

338 (WRF) model, and in this study, the P-X scheme is used. Deposition to wetted cuticular and ground surfaces considers

339 the bulk accommodation coefficient, following Fahey et al. (2017), and can be a limiting factor for highly soluble

340 compounds. The value of R_{inc} follows Shuttleworth and Wallace (1985) as does Massad et al. (2010), but uses the

341 canopy momentum attenuation parameterization from Yi (2008) and in-canopy eddy diffusivity following Harman

342 and Finnigan (2007). This parameterization is similar to Bash et al. (2010), and detailed descriptions of model

343 resistances can be found in the references mentioned above.

344 Dry deposition (F) of aerosol nitrogen (NH_4^+ and NO_3^-) is estimated as the product of the measured concentration

345 (C) and the STAGE modeled dry deposition velocity (V_d):

346
$$F = -V_d(z) \times C(z). \tag{10}$$

347 Aerosol dry deposition processes include gravitational settling, Brownian diffusion, surface impaction, and rebound.

348 Similar to gases, STAGE calculates the averaged V_d for particles by summing the V_d over vegetative or non-vegetative

349   surfaces, weighted by vegetation cover fraction which is = 1 (full coverage) at Coweeta. V_d for a particle with

350   aerodynamic diameter D_p is calculated as:

351    $$V_d(D_p) = \frac{V_g}{1-exp[-V_g(R_a+R_{bp})]} \quad , \tag{11}$$

352   where R_{bp} is the boundary layer resistance for particles, and the gravitational settling velocity (V_g) is calculated as:

353    $$V_g = \frac{\rho D_p^2 g}{18\mu} C_c , \tag{12}$$

354   where ρ is the density of the aerosol, g is the acceleration of gravity, μ is the air dynamic viscosity, and C_c is the

355   Cunningham slip correction factor. The turbulent transport processes are considered similar for gas and aerosol, and

356   R_a can be formulated based on the similarity theory relationships. Unlike deposition of gases, the boundary layer

357   resistance usually dominates the aerosol deposition process as Brownian diffusion is much slower for particles than

358   molecular diffusion is for gases (Pleim and Ran, 2011). Thus, R_{bp} depends on the collection efficiency of the surface

359   and can be determined as:

360    $$R_{bp} = \left[F_f u_* \left(S_c^{-\frac{2}{3}} + E_{im} \right) \right]^{-1} , \tag{13}$$

361   where u_* is the friction velocity, and S_c is the Schmidt number for particles. The quantity E_{im} represents the collection

362   efficiency by impaction and follows Slinn (1982) for vegetative canopies and Giorgi (1986) for smooth (non-

363   vegetative) surfaces. The quantity F_f is an empirical correction factor to account for increased deposition in convective

364   conditions, parameterized as:

365    $$F_f = V_{fac} \left(1 + 0.24 \frac{w_*^2}{u_*^2} \right), \tag{14}$$

366   where V_{fac} is an empirical constant representing the enhanced effects over vegetation canopies. For vegetative

367   canopies, V_{fac} is equal to the one-sided leaf area index (LAI) with a minimum value of one, and for non-vegetative

368   surface, a value of one is used. The quantity w_* is the convective velocity scale (Deardorff velocity), defined as:

369    $$w_* = \left(\frac{g}{T_v} z_i \overline{w't'} \right)^{\frac{1}{3}} , \tag{15}$$

370   where T_v is virtual air temperature, z_i is average depth of the mixed layer, and $\overline{w't'}$ is the measured kinematic surface

371   heat flux.

372   A bulk V_d for $PM_{2.5}$ is obtained by integrating size-resolved V_d according to the particle size distribution. The size

373   distribution profiles for NH_4^+ and NO_3^- are from measurements at eight Canadian rural forest sites (Zhang et al., 2008)

374   and the size distribution for particulate organic nitrogen is estimated as an average of that for NH_4^+ and NO_3^-. Model

375   sensitivities of particle nitrogen fluxes to assumed size distributions are discussed in Supplemental Section S5.

376   The STAGE model is extracted from the CMAQ v5.3 and executed in a one-dimensional mode. The prescribed surface

377   parameters (e.g., z_0, d) were modified according to the site conditions. The continuous LAI data were extracted from

378   the MODerate resolution Imaging Spectroradiometer (MODIS) global LAI product (MCD15A2H), which is generated

379   daily at a 500-m spatial resolution, and each data point covers an 8-d period. The MODIS LAI (Supplemental Figure

380   S6) was adjusted using in-situ canopy measurements as described in Supplemental Section S4. Hourly meteorological

381   measurements, including air temperature, relative humidity, u_*, atmospheric pressure, precipitation rate, global

382   radiation, and soil temperature/moisture, were used to drive STAGE. The Obukhov length, which is defined as:

383    $$L = -\frac{u_*^3 T_v}{(kg\overline{w't'})} \quad ,$$ (16)

384   where k is the von Karman constant, was also calculated from micrometeorological measurements.

385   **2.2.7 Air concentrations for dry deposition modeling**

386   Air concentration data used for dry deposition modeling are summarized in Table 3. Hourly measurements of HNO_3

387   by DD_CL and ΣAN and ΣPN by TD-PC-CL were conducted for a full year and were therefore used directly for

388   modeling. Over the 12-month sampling period, 18%, 22%, and 22% of hourly HNO_3, ΣAN, and ΣPN concentrations

389   were missing or invalid, respectively. Missing data were replaced with the corresponding hour from the median diel

390   profile comprised of days with > 75% completeness. Surrogate formulas of nitrooxy-butanol ($C_4H_9NO_4$) and PAN

391   ($C_2H_3NO_5$) were assumed for ΣAN and ΣPN, respectively.

392   Continuous NH_3 concentrations were only measured during the last two intensives. Biweekly AMoN NH_3

393   measurements, with corrections for travel blanks and atmospheric pressure, were used to establish a continuous 12-

394   month time series of air concentration for annual deposition modeling. Ammonia concentrations are known to exhibit

395   pronounced diel patterns, even in remote areas (Wentworth et al., 2016). Variability in air concentration interacts with

396   diel cycles in surface wetness, turbulence, and other factors to influence diel patterns in air-surface exchange rates. To

397   incorporate this interaction, the diel concentration pattern determined during spring and summer 2016 by MARGA

398   NH_3 measurements (Supplemental Figure S7) was imposed on the biweekly AMoN NH_3 concentration. The hourly

399   profile of NH_3 concentrations was normalized by the corresponding overall mean concentration to produce a

400   normalized mean diel concentration profile. This profile was then applied to each biweekly AMoN air concentration,

401   temporally scaling the NH_3 concentration by time of day while maintaining the measured biweekly AMoN

402   concentration. Gap filling of AMoN data was not required. Comparisons of NH_3 measurements are briefly discussed

403   in Supplemental Section S1.

404   Hi-Vol measurements of speciated particulate N were only conducted during intensive periods to assess the relative

405   contributions of inorganic and organic fractions to total water-soluble N. The CASTNET particulate NH_4^+ and NO_3^-

406   were used to provide a continuous 12-month time series of air concentration for annual deposition modeling.

407   Concentrations of Hi-Vol and CASTNET measurements were shown to be comparable (Supplemental Section S1).

408   For the annual time series, particulate organic nitrogen (PON) concentration was estimated based on speciated

409   measurements during intensives, which showed that inorganic N accounts for ~88% of WSTN on average. Weekly

410   average PON concentration was estimated from the weekly CASTNET measurements assuming $NH_4^+ + NO_3^-$

411   represents 88% of total particulate nitrogen and PON represents the balance (12%). Weekly concentrations were then

412   expressed at the hourly time scale for modeling. Gap filling of CASTNET data was not required.

413   Components of the atmospheric reactive N budget that are not routinely measured at Coweeta and were not directly

414   measured during SANDS include NO, NO_2, HONO, and N_2O_5. At the continental scale, regional model simulations

415   suggest that NO, HONO and N_2O_5 make minor contributions to the total dry deposition of reactive N ($\sim$ 2%), though

416   the contribution of NO_2 is larger (∼ 6%) (Walker et al., 2020). While NO, HONO, and N_2O_5 have been excluded from

417   our modeling analysis, we have included an estimate of NO_2 concentration, from which dry deposition is estimated.

418   The "other" fraction of NO_y (i.e., $NO_y – HNO_3 – \Sigma PN – \Sigma AN$) measured at Coweeta represents between 47% (summer)

419   and 76% (winter) of total NO_y on a seasonal basis. This "other" fraction includes NO, NO_2, HONO, N_2O_5, and some

420   NO_3^- but is likely dominated by NO_2. The measured diel profile of "other" NO_y (Supplemental Figure S8)

421   concentration shows the typical pattern indicative of morning and evening modes related to mobile NOx emissions.

422   Winds at Coweeta are from the east/northeast during the morning, which is the direction of local residences, the town

423   of Otto, NC, and U.S. Highway 23. Winds are from the west/southwest during the evening, which is the direction of

424   the Nantahala National Forest. Consistent with the diel profile of "other" NO_y, a much larger morning peak in NO_2 is

425   therefore expected. To estimate the concentration of NO_2 from the measured "other" NO_y, we examined the ratio of

426   NO_2 to the quantity $NO_y – HNO_3 – PANS – NTR$ (e.g., "other" NO_y) simulated by CMAQ (V5.2.1) for the Coweeta

427   site over the year 2015, where PANS represents total peroxy nitrates, and NTR represents other organic nitrates.

428   Relative to the measured NO_y species, PANS and NTR are assumed to represent ΣPN and ΣAN, respectively. The

429   ratio of CMAQ estimated NO_2 to "other" NO_y ranges from 0.51 during summer to 0.60 during winter. These seasonal

430   factors were applied to the measured "other" NO_y to estimate the hourly NO_2 concentration. Gap filling procedures

431   for hourly "other" NO_y follow those for HNO_3, ΣPN, and ΣAN described above. Details of CMAQ V5.2.1 can be

432   found in Supplemental Table S3.

433   Regarding the use of measurements from different towers (Table 3) for inferential modeling, we acknowledge

434   that differences in tower position on the landscape (i.e., within the forest (EFT) versus adjacent clearing (COW137))

435   and height of the measurement above the surface will be sources of variability in air concentrations. Given the

436   complexity of the topography, no attempt was made to correct air concentrations for differences in measurement

437   heights.

3 Results and discussion

3.1 Long-term trends in atmospheric N at Coweeta

439   Emissions of oxidized nitrogen (NOx) and sulfur (SOx) have declined significantly in the eastern U.S. in response to

440   the 1990 Clean Air Act Amendments (Figure 2). Trends data from U.S EPA's National Emissions Inventory (NEI)

441   indicate a nationwide decline of 74% and 46% for SO_x and NOx emissions from the early 1990s to 2010s, respectively,

442   comparing 1990–1994 to 2010–2014 annual averages (U.S. EPA, 2014). By contrast, NH_3 emissions have been

443   reported as relatively unchanged or slightly increasing for the same periods (Ellis et al., 2013; Paulot and Jacob, 2013;

444   Xing et al., 2013), depending on the location and region of the U.S. Declining NOx and SOx emissions have resulted

445   in decreasing trends in air concentrations of HNO_3 and SO_2 at Coweeta between the1990s and 2010s (Figure 2).

446   Concentrations noticeably began to decline in 2008, the timeline of which likely indicates the effect of full

447   implementation of the 2006 Tier 2 Gasoline Sulfur Program, as well as the enactment of the Clean Air Interstate Rule

448   (CAIR), both of which aimed to further reduce NOx and SOx emissions (Sickles and Shadwick, 2015; LaCount et al.,

449   2021). Compared to other species, NH_3 concentrations have only been measured at Coweeta for a relatively short

450   period of time.

451   Atmospheric NH_3 reacts with acidic sulfate to form ammonium sulfate $((NH_4)_2SO_4)$ or bi-sulfate $((NH_4)HSO_4)$

452   aerosol. Under favorable thermodynamic conditions (low temperature and high RH), NH_3 in excess of acidic sulfate

453   will react with HNO_3 to form ammonium nitrate aerosol (NH_4NO_3). Concentrations of SO_4^{2-} at Coweeta have tracked

454   SO_2, and subsequently, NH_4^+ concentrations have declined substantially relative to early 1990s levels (Figure 2).

455   However, concentrations of NO_3^- aerosol, which are relatively low at Coweeta, have not followed trends in SO_4^{2-} and

456   NH_4^+ (Figure 2). Previous studies at other U.S. sites have also reported non-proportional changes in $PM_{2.5}$ mass in

457   response to SO_2 and NOx control strategies (Blanchard and Hidy, 2005; Sickles and Shadwick, 2015). Non-linear

458   reductions or increases of particulate NO_3^- with coincident SO_2 and NOx emission reductions relate to the

459   thermodynamic equilibrium of the SO_4^{2-}- NO_3^-- NH_4^+-HNO_3-NH_3 aerosol system. As ambient SO_4^{2-} concentrations

460   decline, the capacity for NH_4^+ formation (i.e., neutralization) also decreases, leaving additional NH_3 in the gas phase.

461   Amounts of NH_3 in excess of acidic SO_4^{2-} can subsequently react with HNO_3 to form NH_4NO_3, confounding the

462   relationship between NOx emission reductions and atmospheric NO_3^- concentrations.

463   The long-term trend in NO_3^- wet deposition at Coweeta (Figure 3) has tracked the downward trend in ambient HNO_3

464   concentration. Wet deposition of NH_4^+, however, shows no apparent trend, in contrast to the decline in NH_4^+ aerosol

465   concentration. This pattern may relate to the combined effects of changes in regional NH_3 emissions, aerosol

466   chemistry, and dry deposition rates on the long-term trend in atmospheric NH_3 concentrations. As noted above,

467   declines in SO_2 emissions and SO_4^{2-} aerosol result in less conversion of NH_3 to NH_4^+ aerosol, leaving more NH_3 in

468   the gas phase. Furthermore, reduced air concentrations of acidic species such as SO_2 and HNO_3 result in lower dry

469   deposition rates and subsequently less acidic deposition surfaces, which in turn reduces the deposition velocity (i.e.,

470   increases the atmospheric lifetime) of NH_3 (Sutton et al., 2003). In addition to changes in emissions, these two

471   processes are thought to be at least partly responsible for the increases in NH_3 air concentrations that have been

472   observed in some locations across the U.S. (Butler et al., 2015; Yu et al., 2018; Yao and Zhang, 2019). While there is

473   no discernable trend in NH_3 air concentrations over the relatively short period of record at Coweeta, a decline in wet

474   deposition of NH_4^+ aerosol may have been offset to some extent by increased wet deposition of NH_3 gas (Asman et

475   al., 1995), which is highly soluble, resulting in an overall lack of trend in NH_4^+ wet deposition at Coweeta over time.

476   Similar to other areas in the U.S. (Li et al., 2016), the downward trend in NO_3^- wet deposition has led to an increase

477   in the relative contribution of reduced forms of N (i.e., $NH_x = NH_3 + NH_4^+$) to inorganic wet N deposition at Coweeta

478    $(NH_4^+:NO_3^-$, Figure 3).

479   **3.2 Wet deposition**

480   Of the various forms of N in precipitation, ammonium was the most abundant inorganic species, contributing 47.0%

481   of WSTN in weekly samples ($N = 52$), on average, followed by NO_3^- (41.7%, Figure 4, Supplemental Table S4). The

482   contribution of NO_2^- was negligible. Organic compounds (WSON) contributed 11% of WSTN, on average, which is

483   within the range of values (3% to 33%) reported for other locations in the U.S. (Scudlark et al., 1998; Whitall and

484   Paerl, 2001; Keene at al., 2002; Beem et al., 2010; Walker et al., 2012; Benedict et al., 2013). While concentrations

485 of N compounds were generally higher during warm months, a seasonal pattern in the percent contribution of WSON
486 to WSTN was not apparent. In a previous study at Coweeta (1994–1996), Knoepp et al. (2008) found that organic
487 nitrogen contributed 21% of total nitrogen in bulk (wet + dry) deposition samples. Differences between Knoepp et al.
488 (2008) and SANDS results may be related to interannual variability or trends in rainfall composition over the
489 intervening two decades (e.g., Figure 3) or differences in collection method (wet only versus bulk deposition) or
490 analytical techniques used for total N analysis (persulfate/UV digestion (Walker et al., 2012) versus total Kjeldahl N
491 (Knoepp et al., 2008)).

3.3 Air concentrations of oxidized N

493 The oxidized fraction of reactive nitrogen (NOy) comprises a mixture of gaseous and particulate inorganic (NO, NO_2,
494 N_2O_5, HONO, HNO_3, NO_3^-) and organic compounds. Owing to its large deposition velocity and typical atmospheric
495 concentration, HNO_3 is the primary contributor to dry deposition of inorganic oxidized N (Walker et al., 2020). Much
496 less is known about the dry deposition of oxidized organic nitrogen compounds (Walker et al., 2020). Peroxy nitrates
497 (PNs) and alkyl and multifunctional nitrates (ANs) are formed during the photochemical oxidation of volatile organic
498 compounds (VOCs) in the presence of NOx (NOx = NO + NO_2). While PNs exist in the gas phase, ANs can exist in
499 the gas or particle phase and can be the dominant chemical sink for NO_x in high biogenic VOC (BVOC)/low NO_x
500 environments (Farmer et al., 2008; Browne and Cohen, 2012; Paulot et al., 2012; Browne et al., 2013). Unlike PNs,
501 ANs can also form at night via nitrate radical-induced oxidation of VOC. Further, PNs and ANs have been shown to
502 contribute significantly to the total NO_y budget in geographically diverse rural and forested environments (e.g., Trainer
503 et al., 1993; Nouaime et al., 1998; Farmer et al., 2008; Browne et al., 2013; Toma et al., 2019). Flux measurements at
504 Blodgett Forest, CA, showed that PN dry deposition contributed 4–19% of total N deposition at the site (Wolfe et al.,
505 2009). Chemical transport modeling with current representation of the atmospheric oxidized nitrogen system suggests
506 that PNs and ANs together contribute ~ 6% of total N deposition and ~ 12% of dry N deposition at the U.S. continental
507 scale, compared to ~ 21% and 34% for HNO_3 and ~ 6% and 9% for particulate NO_3^- (Walker et al., 2020).
508 The annual average concentration of NOy was 1.00 ppb (0.55 µg N m^{-3}), with the highest seasonal average
509 concentration in the winter (1.32 ppb, 0.75 µg N m^{-3}) and lowest in the summer (0.64 ppb, 0.34 µg N m^{-3}) (Figure 5,
510 Table S5). The nearest rural NOy monitoring site is 85 km to the northwest at Look Rock in the Great Smoky
511 Mountains National Park, where the annual concentration was 1.5 ppb over the same period (NPS, 2020). Similar to
512 Coweeta, NOy concentrations at Look Rock are typically lowest during summer and highest in winter, though the
513 seasonal cycle exhibits some interannual variability. The annual mean concentrations of HNO_3, ΣPN, ΣAN determined
514 by TD-PC-CL were 0.14 (0.08), 0.1 (0.06), and 0.09 (0.05) ppb (µg N m^{-3}), respectively (Figure 5, Table S5). HNO_3
515 and ΣPN concentrations peaked in spring, coincident with the seasonal peak in O_3 concentration, while concentrations
516 of ΣAN were similar in spring and summer. Diel patterns of HNO_3, ΣPN, and ΣAN peaked during the day as expected
517 for photochemical products. However, of the organic compounds, the ratio of peak daytime to minimum nighttime
518 concentrations (Figure 5) was much smaller for ΣAN (2.3) compared to ΣPN (3.9), possibly indicative of the additional
519 nighttime formation of AN.

520   Annually, HNO$_3$ (12.8%), ΣPN (12.2%), and ΣAN (12.7%) contributed approximately the same proportions of the

521   atmospheric NOy load (Figure 5, Table S6). Their collective contribution (NO$_z$ = HNO$_3$ + ΣPN + ΣAN) to total NOy

522   peaked during the summer (52.9%) and reached a minimum during winter (24.2%). The contributions of ΣPN (16.7%)

523   and ΣAN (20.0%) exceeded HNO$_3$ (16.2%) during summer when total NOy concentrations were lowest. Our results

524   fall within the range of NOy budgets reported for other rural forested sites, in which ΣPN and ΣAN contribute ~ 8–

525   40% (Nouaime et al., 1998; Farmer et al., 2008; Browne et al., 2013; Toma et al., 2019) and 10–22% (Day et al., 2003;

526   Farmer et al., 2008; Browne et al., 2013) of NOy, respectively.

527   To put the SANDS period into context with longer-term variability of oxidized N concentrations at Coweeta,

528   CASTNET HNO$_3$, and NO$_3^-$ measurements for the period 2015–2020 are summarized in Figure 6 along with the

529   SANDS period. We note here that NH$_4$NO$_3$ volatility on the CASTNET Teflon filter can result in positive and negative

530   biases in HNO$_3$ and NO$_3^-$, respectively, with larger biases expected under warmer conditions (Lavery et al., 2009).

531   Studies have shown the total NO$_3^-$ (TNO$_3$ = HNO$_3$ and NO$_3^-$) to be conserved, though some portion of the NO$_3^-$

532   collected by the CASTNET open-faced filter may be contributed by coarse particles. The partitioning of TNO$_3$

533   between gas and particulate phases is important, given the much larger deposition velocity of HNO$_3$ compared to NO$_3^-$

534   . The CASTNET measurements reflect relatively low concentrations of both HNO$_3$ and NO$_3^-$, with HNO$_3$ exceeding

535   NO$_3^-$ during all seasons. Particulate NO$_3^-$ concentrations are highest during cooler months, as expected, and negligible

536   during the summer, a pattern that is consistent with observations from other networks across the Southeast (Kim et

537   al., 2015). Additionally, TNO$_3$ is primarily in the gas phase even during winter. Seasonal mean concentrations during

538   the SANDS period fall within the interquartile range (IQR) of the 6-year period between 2015 and 2020, with SANDS

539   annual and 6-year averages being very similar (Figure 6). Seasonal and annual mean HNO$_3$ concentrations agreed

540   closely with the CASTNET measurements (Figures 6 and Supplemental Section S1).

541   **3.4 Air concentrations of reduced N**

542   Reduced forms of nitrogen (NH$_x$) represent another important component of the inorganic dry N deposition budget.

543   At the continental scale, NH$_3$ dry deposition contributes ~ 20% of total N deposition and ~ 32% of dry N deposition,

544   whereas the contributions from NH$_4^+$ aerosol are ~ 4% and ~ 6%, respectively (Walker et al., 2020). Similar to oxidized

545   forms of N, the partitioning of mass between the gas (NH$_3$) and particulate (NH$_4^+$) phases affects the dry deposition

546   rate of NH$_x$, given the larger deposition velocity of NH$_3$ relative to NH$_4^+$.

547   During 2015–2020, with 2020 being the most recent full year of AMoN data, average concentrations of NH$_3$ and NH$_4^+$

548   were similar (Figure 7). Both species displayed a seasonal pattern of lowest concentrations in the winter and higher

549   concentrations during warm months. NH$_3$ concentrations peaked in summer, reflecting the temperature dependence

550   of regional agricultural and biogenic emissions. NH$_4^+$ concentrations followed the seasonal cycle in SO$_4^{2-}$

551   concentrations, which were also similar in spring and summer and minimum in winter at Coweeta. The seasonal cycle

552   of NH$_3$/NH$_4^+$ partitioning was driven more by NH$_3$ than NH$_4^+$, the former exhibiting more seasonal variability. Hourly

553   measurements conducted during spring and summer 2016 showed that NH$_3$ also displayed significant diel variability

554   (Supplemental Figure S7), reaching a maximum around mid-day and minimum overnight. Seasonal mean

555   concentrations during the SANDS period fall within the IQR of the 6-year period between 2015 and 2020, with

556 SANDS annual and 6-year averages being very similar. Concentrations of NH_x were higher relative to TNO_3 during

557 SANDS and over the longer term at Coweeta (Figures 6 and 7).

3.5 Aerosol N composition

559 Ammonium was the most abundant inorganic species, contributing 86.8% of WSTN ($N = 103$) on average (Figure 8,

560 Table S7). Organic compounds (WSON) contributed 11.5% of WSTN, which is very similar to precipitation. The

561 contributions of NO_3^- and NO_2^- were minor. Our study-wide average of %WSON is slightly lower than measurements

562 at other North American forest sites, including Duke Forest, North Carolina (~33%, Lin et al., 2010) and Rocky

563 Mountain National Park (14–21%) (Benedict et al., 2012), but is within the global range of 10–39% (Cape et al.,

564 2011). Similar to precipitation chemistry, there was no seasonal pattern in the percent contribution of WSON to WSTN

565 in $PM_{2.5}$. Hi-Vol measurements of inorganic PM components compared well, overall, with collocated CASTNET

566 measurements (Supplemental Section S1).

3.6 Biogeochemistry

568 Estimates of NH_3 emission potentials (Γ) for the ground and vegetation are needed to calculate compensation points

569 (χ) and fluxes in STAGE. Measurements of pH, NH_4^+ and corresponding Γ of the leaves (Γ_s) and litter (Γ_l) are

570 summarized in Figure 9 and Supplemental Tables S8 and S9. Measurements of Γ_s are divided into green leaves

571 collected during the growing season (spring and summer) and senescent leaves collected in October. NH_3 emission

572 potentials (Γ) for green leaves (Γ_s) ranged from zero to 4070 with a median value (35.8) (Table S8) corresponding to

573 a compensation point of $\chi_s = 0.25$ μg NH_3 m^{-3} at 25 °C. Large intra-species variability of tissue pH and NH_4^+ were

574 observed (Table S9) and separating by crown versus understory species did not reveal distinct differences between

575 groups. Given the variability of the observations, the median Γ_s was used for STAGE simulations. Senescence marks

576 the translocation of N in leaves to storage tissues (Schneider et al., 1996). Along with a decline in photosynthetic

577 activity, degradation of chlorophyll, and other metabolic changes, glutamine synthetase (GS) activity also declines

578 (Pearson et al., 2002). Glutamine synthetase catalyzes assimilation of NH_4^+ into glutamine and is therefore important

579 in regulating the pool of NH_4^+ available for exchange as NH_3 between the leaf and atmosphere and remobilizing

580 organic N for storage during senescence. A decline in GS activity can thus result in increased leaf NH_4^+ concentrations

581 (Pearson et al., 2002; Wang et al., 2011). Senescent leaves were similar to green leaves with respect to median tissue

582 pH but showed distinctly higher concentrations of tissue NH_4^+. Median Γ_s was correspondingly higher (113),

583 equivalent to $\chi_s = 0.8$ μg NH_3 m^{-3} at 25 °C. For STAGE modeling, the median Γ for senescent leaves was used for Γ_s

584 during the fall.

585 Regard our method for estimating Γ_s, the fundamental assumption is that the chemistry of the bulk leaf tissue is

586 representative of the apoplast. While a number of studies have shown positive correlations between bulk tissue

587 chemistry, apoplastic chemistry, and independently quantified compensation points (David et al., 2009; Hill et al.

588 2002; Massad et al. 2010; Mattsson and Schjoerring 2002; Mattsson et al. 2009), absolute differences between Γ_s

589 derived from bulk tissue versus apoplast measurements can be large. For example, Sutton et al. (2009) and Personne

590 et al. (2015) both show that ratios derived from bulk tissue chemistry exceed those derived from apoplast chemistry.

591 We did not perform experiments to validate the use of bulk tissue chemistry as a proxy for apoplast chemistry and

592 acknowledge this source of uncertainty. However, our estimates of Γ_s appear reasonable in the context of the range of

593 existing observations (cited above and summarized by Massad et al., 2010) and the general relationship between

594 $[NH_4^+]_{bulk}$ and Γ_s put forth by Massad et al. (2010, equation 6). Measurements on bulk tissue are less labor intensive

595 and therefore more tempting than measurements on the apoplast. However, more studies comparing to two procedures

596 are needed to extend the meta-analysis of Massad et al. (2010) to a wider range of natural ecosystems, particularly

597 deciduous forests.

598 Leaf litter on the soil surface has been shown to be a source of NH_3 to the atmosphere in both natural and agricultural

599 ecosystems (Nemitz et al., 2000b; David et al., 2009; Hansen et al., 2013). As litter decomposes, mineralization of

600 organic N is a source of NH_4^+, some of which is lost to the overlying air as NH_3. Litter NH_4^+ concentrations were

601 similar to green leaves but lower than senescent leaves (Figure 9). However, the pH was higher than both green and

602 senescent leaves. The resulting median Γ_l (69.3) was larger than green leaves but smaller than senescent leaves,

603 equivalent to $\chi_l = 0.49$ µg NH_3 m^{-3} at 25 °C. Litter Γ was much larger than that of the underlying soil. Average (0–10

604 cm soil depth) soil pH (4.18) and NH_4^+ (1.21 mg N kg^{-1}) correspond to $\Gamma_{soil} \sim 10$ at a soil mass wetness of 0.1 g g^{-1},

605 equivalent to $\chi_{soil} \sim 0.1$ µg NH_3 m^{-3} at 25 °C. This very low Γ_{soil} results from the low pH of the shallow soil.

606 Vertical profiles of air concentrations within and above the canopy were measured to investigate patterns of air-surface

607 exchange with specific ecosystem compartments (i.e., canopy crown, understory, and ground). A detailed analysis of

608 bi-directional N fluxes is forthcoming; thus, we limit the discussion of these data to NH_3 in the context of interpreting

609 patterns observed in the biogeochemical emission potentials and their prescription in the STAGE model. Nitric acid,

610 NH_4^+, and NO_3^- showed expected decreasing concentrations from above the canopy to the forest floor, indicative of

611 deposition. While NH_3 profiles showed patterns of deposition to the crown and understory, concentrations near the

612 forest floor indicated both emissions and deposition (Figure 10). Of the 76 daytime profiles measured, 40% showed

613 decreases down to the forest floor, and 60% showed increasing concentration from approximately the lower understory

614 (~ 5 m above ground) to the forest floor. The former pattern is interpreted as deposition to the forest floor, and the

615 latter is interpreted as emission. Thus, the mean profile suggests a source of NH_3 at the ground. The very low Γ_{soil}

616 suggests that emission from the soil is unlikely given such a low pH. The leaf litter layer, which indicates a much

617 higher emission potential (Γ_l) than the soil, is a more likely source of NH_3. This hypothesis is consistent with Hansen

618 et al. (2013; 2017), in which emissions of NH_3 from a beech (*Fagus sylvatica*) forest after leaf fall were attributed to

619 the decomposition of new litter. Similar to our site, the underlying soil also had low pH (4–5). Given our observations,

620 we used Γ_l (median = 69.3, Table S8) rather than Γ_{soil} as the ground emission potential (Γ_g) in STAGE.

621 **3.7 N deposition budget**

622 Total annual N deposition for the period August 2015 – August 2016 was 6.7 kg N ha^{-1} (Figure 11). Over this period,

623 wet deposition contributed 60.7% of total N deposition, of which NH_4^+ was the primary component (29.6%). Wet

624 deposition of organic N contributed 5.4% of the total N deposition budget. Dry deposition accounted for 39.3% of

625 total deposition, of which NH_3 was the primary contributor (20.6%). Reduced forms of inorganic N were the largest

contributor to the budget (51.2%), with oxidized inorganic and organic N contributing 41.2% and 7.6% of total N deposition, respectively. Dry deposition of organic N made a small contribution (2.2%) to the total deposition budget. Ammonia is the most important contributor to the dry deposition budget (52.3%) and differs from the other species in that it is exchanged bidirectionally between the ground, canopy and atmosphere.

Seasonal net canopy-scale and component fluxes are shown in Supplemental Figure S9. The mean net flux (F_{net}) is downward (i.e., deposition) during all seasons, generally following the seasonal pattern of the atmospheric NH_3 concentration. The cuticular flux (F_{cut}), which is unidirectional in STAGE, is the dominant deposition pathway and ranged from -97.7 ng N m^{-2} s^{-1} (deposition) to near zero. The contribution of F_{cut} to the total net flux ranged from 84.7% in spring to ~ 100% during fall. The stomatal flux (F_s) is bidirectional, ranging from -4.5 ng N m^{-2} s^{-1} (deposition) to 2.3 ng N m^{-2} s^{-1} (emission), with the largest fluxes occurring during warmer periods of the growing season when the stomatal resistance is lowest. The stomatal flux is smaller than F_{cut} for several reasons. First, R_s is generally larger than R_{cut}. Also, in the current model formulation the cuticular compensation $X_{cut} = 0$. Thus, the NH_3 concentration gradient between air above the leaf (X_{leaf}) and X_s is smaller than for X_{cut}. Finally, low LAI and large R_s in winter and fall and offsetting bidirectional fluxes in spring and summer result in a relatively small mean stomatal deposition flux (F_s) across seasons. F_g is also bidirectional, ranging from -3.9 ng N m^{-2} s^{-1} (deposition) to 2.5 ng N m^{-2} s^{-1} (emission). Fluxes are largest during spring as atmospheric NH_3 begins to increase with warmer temperatures but before peak LAI is reached, after which the denser canopy increases the in-canopy aerodynamic (R_{inc}) and air-side ground boundary-layer resistances (R_{bg}) (Table S2), thereby decreasing F_g. On an annual scale, F_g and F_s make similar contributions to (~ 3.0%) to F_{net}.

Nitric acid was the second largest component of dry deposition, contributing 36.2% of the total. While HNO_3 deposits more rapidly than NH_3 (Supplemental Table S10), the overall importance to the dry N budget is constrained by relatively low air concentrations at this remote forest site. Particulate species made much smaller contributions to the budget due to much lower deposition velocities (V_d = flux/air concentration) relative to their gaseous counterparts (Supplemental Table S10). For example, while NH_4^+ contributed more to the atmospheric NH_x load than NH_3, (Figure 7), the NH_x flux budget was regulated by the much more rapid exchange of NH_3 between the forest and atmosphere relative to NH_4^+. A similar example was observed for oxidized N. While NO_2 represents an important fraction of the oxidized N concentration budget via its contribution to "Other NOy", NO_2 deposits much less rapidly than HNO_3 (Supplemental Table S10) thereby contributing a relatively small fraction (3.0%) of the dry N flux. Of the organic N species, AN contributed slightly more (2.9%) to dry N deposition than PN (2.3%) owing to a higher deposition velocity (Supplemental Table S10). Similar to particulate NH_4^+ and NO_3^-, PON made a small contribution to dry N deposition (0.4%) due to its low V_d (Supplemental Table S10). Reduced forms of N accounted for the majority of dry N deposition (55.1%), with oxidized inorganic and organic forms of N contributing 39.4% and 5.5%, respectively.

Total N deposition peaked during the summer (2.5 kg N ha^{-1}) and reached a minimum in the fall (1.0 kg N ha^{-1}) (Figure 12). Wet deposition exceeded dry deposition during all seasons. Seasonal variability in wet deposition was primarily driven by precipitation amount, whereas dry deposition was influenced by seasonality in air concentrations of the primary N_r species (Figures 6 and 7), LAI (Figure S6), turbulence, and other surface characteristics. Ammonia fluxes followed the seasonal pattern of air concentration, peaking in the summer and reaching a minimum in winter.

663 Concentrations and fluxes of HNO_3 peaked in the spring and reached a minimum in the fall. Deposition velocities,

664 which can be thought of as the concentration-normalized flux, peaked during the summer and reached a minimum

665 during winter for most N species. This pattern likely reflects the combined effect of seasonal cycles in LAI and

666 turbulence characteristics. The seasonal pattern of V_d for HNO_3 differed slightly from the other species, peaking in

667 spring and reaching a minimum in fall. In contrast to other N species, HNO_3 deposition is limited by turbulent transfer,

668 the canopy (surface) resistance being zero. The pattern of HNO_3 V_d thus partially reflects seasonal patterns in wind

669 speed and degree of turbulent mixing above the canopy.

3.8 Evaluation of the dry deposition model

671 While total uncertainty in the dry deposition budget cannot be rigorously quantified (Walker et al., 2019a), the

672 sensitivity of the model to parameterizations and key inputs can elucidate important aspects of model uncertainty and

673 inform a potential range of dry deposition estimates. Here we undertake such an exercise, evaluating several alternative

674 modeling scenarios to assess the sensitivity of fluxes and total dry deposition to assumptions regarding LAI, NH_3

675 emission potentials ($\Gamma_{s,l}$), NH_3 cuticular resistance ($R_{cut,dry}$), and particle size distribution. We focus on NH_3, as it is

676 the most important component of the dry deposition budget and more complex with regard to air-surface exchange

677 processes than the other species. Sensitivity tests are summarized in Supplemental Section S5 and Table S11. Of the

678 scenarios tested, increasing Γ_l and Γ_s within the range of observations and reducing $R_{cut,dry}$ within the variability

679 reported by Massad et al. (2010) exerted the largest control over the dry deposition flux, establishing a range of total

680 dry deposition from 2.0 (increasing $\Gamma_{s,l}$) to 3.1 (decreasing $R_{cut,dry}$) kg N ha^{-1} around the base value of 2.6 kg N ha^{-1}.

681 The corresponding % contribution of NH_3 to total dry N deposition ranges from 36.6% to 58.5% (base = 52%) and

682 the contribution of dry to total wet + dry deposition ranges from 33.0% to 43.0% (base = 39.4%). Our results point to

683 the need for a better understanding of the processes of cuticular exchange and the importance of adequately

684 characterizing the magnitude and variability of vegetation and litter emission potentials in forests.

685 Another method of evaluating model behavior is the comparison with measured V_d. During the final summer intensive,

686 a small dataset ($N = 19$ observations) of V_d was determined from daytime measurements of vertical concentration

687 gradients above the canopy using the MBR method. Measured V_d was compared to V_d derived from the STAGE model

688 for overlapping periods, and the maximum possible V_{dmax} as $1/(R_a + R_b)$. Of the 19 MBR measurements, four NH_3

689 profiles exhibited emissions (6.8 to 22.4 ng NH_3 m^2 s^{-1}), which were not reproduced by STAGE. Analysis of the

690 meteorological conditions during the MBR measurements suggests that emissions tend to occur during the warmest

691 periods with lowest relative humidity. This would correspond to periods when R_{cut} and X_s are high and may indicate

692 that the model is underestimating F_s emissions during these periods. Excluding the four emission periods, V_d estimated

693 from MBR and STAGE agree reasonably well (Supplemental Figure S11). As is the case for STAGE, resistance-based

694 models typically assume HNO_3 deposits at the rate of V_{dmax} (i.e., $R_c = 0$). As shown in Figure S11, fluxes measured

695 during summer 2016 showed MBR V_d for HNO_3 larger than NH_3, as expected, but lower than V_{dmax}. This apparent

696 non-zero R_c could result from a real non-zero R_c caused, for example, by equilibrium of HNO_3 and NO_3^- on leaf

697 surfaces (Nemitz et al., 2004a). This pattern may also reflect the influence of flux divergence related to NH_4NO_3

698 evaporation in the canopy crown, which would reduce the magnitude of the downward vertical gradients, and therefore

699   the measured V_d, of HNO_3 and NH_3 (Nemitz et al., 2004b). In this study, concentrations of NO_3^- (mean = 0.08 μg m$^-$

700   ^{3}) were much lower than HNO_3 (mean = 0.47 μg m^{-3}), and NO_3^- gradients were therefore difficult to resolve, precluding

701   a definitive explanation of HNO_3 $V_d < V_{dmax}$. Ignoring potentially significant uncertainties related to the measurement

702   of chemical and temperature gradients within the roughness sublayer, our results suggest that periods of NH_3 emission

703   during the day, particularly at higher air temperature and lower humidity, may be underestimated. Our results also

704   reinforce the need for temporally extensive measurements of concentrations and fluxes of HNO_3, NH_3, and NO_3^- to

705   examine exchange processes and uncertainties related to chemical flux divergence.

706   **3.9 Spatial and temporal representativeness of deposition budget**

707   The complexity of atmospheric flows in mountainous terrain influences the spatial variability of wet and dry

708   deposition processes (Lehner and Rotach, 2018). As the deposition budget presented above is based on measurements

709   from the lowest elevation portion of the Coweeta basin, the degree to which the budget is spatially representative must

710   be consisdered. Potential effects on dry deposition were assessed by characterizing the magnitude and spatial

711   variability of HNO_3 and NH_3 concentrations along an elevation gradient (Figure 1, Table 1) from the lower to upper

712   portions of the Coweeta Basin. It should be noted that HNO_3 concentrations at NC25 were measured by CASTNET

713   while HNO_3 passive samplers were used at the other locations. Concentrations are summarized in Figure 13, in which

714   the sites are ordered left to right from lowest to highest elevation. Nitric acid and NH_3 concentrations increase slightly

715   with elevation, an explanation for which is not obvious. Nitric acid concentrations are highest at Screwdriver Knob,

716   which is distinct from the other sites in that the measurement tower was situated on a relatively narrow exposed ridge.

717   The measurements are therefore higher above the surrounding vegetation than at the other sites. Overall, variability

718   of air concentrations across sites, even including SK, is sufficiently small such that spatial variability of dry deposition

719   across the basin would likely be driven more by variability in meteorology than air concentrations.

720   A quantitative assessment of the effects of air flow on dry deposition across the basin is not possible, but the work of

721   Hicks (2008) illustrates the relevant effects in the context of the resistance analogy for V_d. Over flat homogeneous

722   terrain, flux to the vegetation is driven by turbulent diffusion in the vertical direction above the canopy and horizontal

723   advection is assumed to be zero. In the extreme case of air flow approaching a steep forested slope, horizontal flow

724   penetrates the canopy and the transfer of material (deposition) to the canopy elements becomes dominated by

725   horizontal advection and filtration rather than vertical diffusion. In the context of V_d, this situation is analogous to the

726   aerodynamic resistance (R_a) approaching zero. Taking HNO_3 as an example under the typical assumption that the

727   canopy resistance (R_c) = 0, V_d becomes limited by the quasi-laminar boundary layer resistance at the vegetation

728   surfaces (R_b). Following the analysis of Hicks et al. (2008), V_d for HNO_3 could be enhanced by a factor of $[1+(R_a/R_b)]^{1/2}$

729   (Hicks, 2008). Using median values of R_a and R_b from our modeling period, this would increase V_d for HNO_3 by a

730   factor of ~ 1.4. For gases that have a significant R_c, enhancements will be smaller. Topographical relief across the

731   Coweeta Basin may be gentle enough such that the flow separation described in the previous example is limited to

732   certain areas and meteorological scenarios. However, as Hicks (2008) points out, flow complexity in mountainous

733   areas has the overall effect of increasing V_d, with areal weighted fluxes being highly dependent on the topographical

734   characteristics specific to the study area. Other effects related to katabatic flows (Novick et al., 2016) and diel patterns

735   of hillside shading that drive temperature-related processes such as NH_3 compensation points introduce additional
736   uncertainties.
737   The results of Knoepp et al. (2008) show that spatial patterns of wet deposition across the Coweeta Basin follow
738   patterns of precipitation amount, which increase with elevation. In their study, bulk deposition of NH_4^+, NO_3^- and total
739   organic nitrogen was measured from 1994–1996 at sites ranging in elevation from 788 to 1389 m. Annual precipitation
740   depth and bulk deposition increased by 25% from the lowest to the highest elevation. This increase in precipitation
741   with elevation is consistent with the 75-year analysis of Coweeta climatological data by Laseter et al. (2012), which
742   showed annual precipitation amount at 1398 m was 32% greater than at 686 m. In our study, wet deposition was
743   measured at the NC25 site at 686 m and therefore represents a lower wet deposition rate than would occur in higher
744   elevation portions of the basin. An approximate 35% enhancement in both wet and dry deposition for the highest
745   elevations within the basin would correspond to a total N deposition rate of 9.0 kg N ha^{-1} yr^{-1} based on our estimate
746   of 6.7 kg N ha^{-1} yr^{-1} for the lower basin.
747   Regarding the temporal representativeness of the deposition budget calculated here, wet deposition of inorganic N
748   (NO_3^- + NH_4^+) during our 12-month model period (3.69 kg N ha^{-1}) agrees well with the mean annual deposition rate
749   measured at NTN site NC25 (3.72 kg N ha^{-1}) over the period 2015–2020, with 2020 being the most recent full year of
750   reported observations. Air concentrations of NO_3^- and HNO_3 (Figure 6) as well as NH_3 and NH_4^+ (Figure 7) during
751   our model period are also similar to the 6-year (2015–2020) mean concentrations measured by CASTNET and AMoN.
752   In this context, our results are deemed temporally representative of the most recently available complete years of
753   monitoring data.

4 Conclusions

754   Due to the success of the Clean Air Act, air concentrations and wet deposition of reactive N at Coweeta are the lowest
755   observed since the beginning of routine monitoring in the late 1970s. However, even at historically low levels, our
756   results show that N_r deposition remains highly ecologically relevant in the context of critical loads. Our estimate of
757   total N_r deposition of 6.7 kg N ha^{-1} yr^{-1} is near the upper-end estimate of mass balance derived critical loads (2.8 to 7
758   kg N ha^{-1} yr^{-1}) recently reported for spruce-fir, beech, and mixed deciduous forests by Pardo et al. (2018) in nearby
759   Great Smoky Mountains National Park. Our result also falls within the range of empirical critical loads of N for
760   combined tree health and biogeochemical responses (3–8 kg N ha^{-1} $yr^{-1)}$ and changes in mycorrhizal fungi spore
761   abundance, community structure and community composition (5–12 kg N ha^{-1} yr^{-1}) in eastern temperate forests (Pardo
762   et al., 2011).
763   A key feature of the deposition budget derived for Coweeta is the predominance of reduced forms (NH_x) of inorganic
764   nitrogen (51.2%) over oxidized inorganic N (41.2%). Reductions in deposition of NH_x will be needed to achieve the
765   lower-end estimates of critical N loads (~ 3 kg N ha^{-1} $yr^{1)}$ for southern Appalachian forests. This presents a challenge,
766   as emissions and air concentrations of NH_3 remain unregulated. Our results also show that organic forms of N make
767   a non-trivial contribution (7.6%) to total N deposition, primarily via wet deposition. It is noted, however, that the gas-
768   phase dry component of deposition only considers oxidized forms as alkyl and peroxy nitrates, excluding contributions
769   from reduced (i.e., NH) organic compounds. While our results represent an advancement in accounting for organic

770 dry N_r deposition in total N_r deposition, the application of new measurement technologies (Walker et al., 2019b) for
771 broader chemical speciation of organic forms of dry N_r deposition is needed.

772 Our results underscore the need for long-term measurements of reactive chemical fluxes, and the coupling of
773 atmospheric and biogeochemical measurements, to improve air-surface exchange models. Novel measurements that
774 more directly elucidate the role of cuticular exchange of NH_3 and more temporally extensive measurements of leaf
775 NH_3 emission potentials are particularly needed. For forest ecosystems, a physically representative parameterization
776 for resistance to NH_3 diffusion through the leaf litter layer and more temporally extensive measurements of the litter
777 NH_3 emission potential combined with more thorough understanding of litter decay dynamics are also needed. For
778 sensitive ecosystems located in mountainous and other topographically complex landscapes, which includes much of
779 the Class I wilderness area in the U.S., identification of locations suitable for micrometeorological flux measurements
780 will be challenging. Novel flux measurement methods and application of in-situ models, including translation of
781 measurements from more ideal to complex locations, will likely be needed. Furthermore, long-term flux datasets are
782 needed to assess the interactive effects of changing air quality and climate on both atmosphere-biosphere exchange
783 and ecosystem response to deposition (e.g., Van Houtven et al., 2019).

Author Contributions

784 1. John T. Walker: Conceptualization, formal analysis, methodology, funding acquisition, project administration,
785 validation, visualization, writing
786 2. Xi Chen: Formal analysis, investigation, methodology, validation, writing
787 3. Zhiyong Wu: Formal analysis, investigation, methodology, software validation, writing
788 4. Donna Schwede: Investigation, formal analysis
789 5. Ryan Daly: Investigation, formal analysis, validation
790 6. Aleksandra Djurkovic: Data curation, investigation, methodology, resources
791 7. A. Christopher Oishi: Conceptualization, formal analysis, methodology, validation
792 8. Eric Edgerton: Data curation, funding acquisition, formal analysis, methodology, validation, resources
793 9. Jesse Bash: Formal analysis, methodology, software
794 10. Jennifer Knoepp: Data curation, investigation
795 11. Melissa Puchalski: Conceptualization, funding acquisition, resources
796 12. John Iiames: Formal analysis, investigation, writing
797 13. Chelcy F. Miniat: Conceptualization, funding acquisition, resources, writing

Disclaimer

798 The views expressed in this article are those of the authors and do not necessarily represent the views or policies of
799 the U.S. EPA. This study was funded in part by the USDA Forest Service, Southern Research Station, Coweeta
800 Hydrologic Lab. The findings and conclusions in this publication are those of the authors and should not be construed
801 to represent any official USDA or U.S. Government determination or policy.
802
803 The authors declare they have no conflict of interest.

Acknowledgements

804 We gratefully acknowledge field and laboratory support from USDA Forest Service staff at the Coweeta Hydrologic
805 Laboratory, including Christine Sobek, Patsy Clinton, Chuck Marshall, and Cindi Brown. David Kirchgessner (retired,
806 U.S. EPA) tirelessly supported field and laboratory activities during SANDS intensives. Lee Nanny (former U.S. EPA)
807 and Mark Barnes (U.S. EPA) supported field intensives and logistics. We also appreciate the support of Kevin Mishoe
808 (Wood, Inc.) and Christopher Rogers (Wood, Inc.) for support of CASTNET field activities and data management,
809 respectively.

810

811

812

813

814

815

References

816 Altieri, K.E., Turpin, B.J., and Seitzinger S.P., 2009. Composition of dissolved organic nitrogen in continental
817 precipitation investigated by Ultra-High Resolution FT-ICR Mass Spectrometry. Environmental Science and
818 Technology 43, 6950-6955.

819 Altieri, K.E., Hastings, M.G., Peters, A.J., Sigman, D.M., 2012. Molecular characterization of water soluble organic
820 nitrogen in marine rainwater by ultra-high resolution electrospray ionization mass spectrometry. Atmospheric
821 Chemistry and Physics 12. 3557-3571.

822 Appel, K.W., Bash, J.O., Fahey, K.M., Foley, K.M., Gilliam, R.C., Hogrefe, C., Hutzell, W.T., Kang, D., Mathur, R.,
823 Murphy, B.N., Napelenok, S.L., Nolte, C.G., Pleim, J.E., Pouliot, G.A., Pye, H.O.T., Ran, L., Roselle, S.J.,
824 Sarwar, G., Schwede, D. B., Sidi, F.I., Spero, T.L., Wong, D.C., 2021. The Community Multiscale Air Quality
825 (CMAQ) model versions 5.3 and 5.3.1: system updates and evaluation. Geoscientific Model Development, 14,
826 2867–2897.

827 Asman, W.A.H., 1995. Parameterization of below-cloud scavenging of highly soluble gases under convective
828 conditions. Atmospheric Environment, 29, 1359-1368.

829 Bash, J.O., Walker, J.T., Katul, G.G., Jones, M.R., Nemitz, E., Robarge, W.P., 2010. Estimating in-canopy ammonia
830 sources and sinks in a fertilized *Zea mays* field. Environmental Science and Technology, 44, 1683-1689.

831 Beem, K.B., Raja, S., Schwandner, F.M., Taylor, C., Lee, T., Sullivan, A.P., Carrico, C.M., McMeeking, G.R., Day,
832 D., Levin, E., Hand, J., Kreidenweis, S.M., Malm, W.C., Collett Jr., J.L., 2010. Deposition of reactive nitrogen
833 during the Rocky Mountain Airborne Nitrogen and Sulfur (RoMANS) Study. Environmental Pollution, 158, 862-
834 872.

835 Benedict, K.B., 2012. Observations of atmospheric reactive nitrogen species and nitrogen deposition in the Rocky
836 Mountains (Thesis). Colorado State University. Libraries.

837   Benedict, K.B., Day, D., Schwandner, F.M., Kreidenweis, S.M., Schichtel, B., Malm, W.C., Collett, J.L., 2013.
838   Observations of atmospheric reactive nitrogen species in Rocky Mountain National Park and across northern
839   Colorado. Atmospheric Environment, 64, 66-76.

840   Blanchard, C.L., Hidy, G.M., 2005. Effects of SO_2 and NOx emission reductions on PM2.5 mass concentrions in the
841   Southeastern United States. Journal of Air and Waste Management Association, 55, 265-272.

842   Bobbink, R., Hornung M., and Roelofs, J.M., 1998. The effects of air-borne nitrogen pollutants on species diversity
843   in natural and semi-natural European vegetation. Journal of Ecology, 86, 717-738.

844   Boonstra, R., Krebs, C.J., Cowcill, K., 2017. Responses of key understory plants in the boreal forests of western North
845   America to natural versus anthropogenic nitrogen levels. Forest Ecology and Management, 401, 45-54.

846   Bragazza, L., Freeman, C., Jones, T., Rydin, H., Limpens, J., Fenner, N., Ellis, T., Gerdol, R., Hajek, M., Iacumin, P.,
847   Kutnar, L., Tahvanainen, T., and Toberman, H., 2006. Atmospheric nitrogen deposition promotes carbon loss
848   from peat bogs. Proceedings of the National Academy of Sciences, 103, 19386-19389.

849   Browne, E.C., Cohen, R.C. 2012 Effects of biogenic nitrate chemistry on the NOx lifetime in remote continental
850   regions. Atmospheric Chemistry and Physics, 12, 11917–11932, doi:10.5194/acp-12-11917-2012.

851   Browne, E.C., Min, K.-E., Wooldridge, P.J., Apel, E., Blake, D.R., Brune, W.H., Cantrell, C.A., Cubison, M.J., Diskin,
852   G.S., Jimenez, J.L., Weinheimer, A.J., Wennberg, P.O., Wisthaler, A., Cohen, R. C., 2013. Observations of total
853         $RONO_2$ over the boreal forest: NOx sinks and HNO_3 sources. Atmospheric Chemistry and Physics, 13, 4543–
854   4562.

855   Butler, T., Vermeylen, F., Lehmann, C.M., Likens, G.E., Puchalski, M. 2016. Increasing ammonia concentration
856   trends in large regions of the USA derived from the NADP/AMoN network. Atmospheric Environment, 146, 132-
857   140.

858   Bytnerowicz, A., Sanz, M.J., Arbaugh, M. J., Padgett, P.E., Jones,D.P., Davila, A., 2005. Passive sampler for
859   monitoring ambient nitric acid (HNO_3) and nitrous acid (HNO_2) concentrations. Atmospheric Environment 39,
860   2655-2660.

861   Caldwell, P., Muldoon, C., Ford Miniat, C., et al., 2014. Quantifying the role of National Forest System lands in
862   providing surface drinking water supply for the Southern United States. Gen. Tech. Rep. SRS-197. Asheville,
863   NC: U.S. Department of Agriculture Forest Service, Southern Research Station. 135 p.

864   Cape, J.N., Cornell, S.E., Jickells, T.D., Nemitz, E., 2011. Organic nitrogen in the atmosphere-Where does it come
865   from? A review of sources and methods. Atmospheric Research 102, 30-48.

866   Chen, F., Dudhia, J., 2001. Coupling an advanced land surface-hydrology model with the Penn State-NCAR MM5
867   modeling system. Part I: Model implementation and sensitivity. Monthly Weather Review, 129, 569-585.

868   Chen, X., Walker, J.T., Geron, C., 2017. Chromatography related performance of the Monitor for AeRosols and GAses
869   in ambient air (MARGA): laboratory and field-based evaluation. Atmospheric Measurement Techniques, 10,
870   3893-3908.

871   Chen, X., Xie, M., Hays, M.D., Edgerton, E., Schwede, D., Walker, J.T., 2018. Characterization of organic nitrogen
872   in aerosols at a forest site in the southern Appalachian Mountains. Atmospheric Chemistry and Physics, 18, 6829-
873   6846.

Clark, C.M., Phelan, J., Doraiswamy, P., Buckley, J., Cajka, J.C., Dennis, R.L., Lynch, J., Nolte, C.G., Spero, T.L., 2018. Atmospheric deposition and exceedances of critical loads from 1800-2025 for the conterminous United States. Ecological Applications, 28, 978-1002.

Cowan, N., Nemitz, E., Walker, J.T., et al., 2022. Review of methods for assessing deposition of reactive nitrogen pollutants across complex terrain with focus on the UK. DOI: 10.1039/D2EA00012A (Critical Review) Environmental Science: Atmospheres.

Coweeta Hydrologic Laboratory 2016. Procedures for chemical analysis. https://www.srs.fs.usda.gov/coweeta/tools-and-data/wetlab-cookbook_revised-2016-01-08.pdf

David, M., Loubet, B., Cellier, P., Mattsson, M., Schjoerring, J.K., Nemitz, E., Roche, R.,Riedo, M., Sutton, M.A., 2009. Ammonia sources and sinks in an intensively managed grassland canopy. Biogeosciences 6, 1903–1915.

Day, D.A., Wooldridge, P.J., Dillon, M. B., Thornton, J.D., and Cohen, R.C., 2002. A thermal dissociation laser-induced fluorescence instrument for in situ detection of NO_2, peroxy nitrates, alkyl nitrates, and HNO_3. Journal of Geophysical Research - Atmospheres, 107, 4046-4059.

Day, D.A., Dillon, M.B., Wooldridge, P.J., Thornton, J.A., Rosen, R.S., Wood, E.C., Cohen, R.C., 2003. On alkyl nitrates, O_3, and the "missing NOy", Journal of Geophysical Research - Atmospheres, 108, 4501.

Doney, S.C., Mahowald, N., Lima, I., Feely, R.A., Mackenzie, F.T., Lamarque, J-F., Rasch, P.J., 2007. Impact of anthropogenic atmospheric nitrogen and sulfur deposition on ocean acidification and the inorganic carbon system. Proceedings of the National Academy of Sciences 104, 14580-14585.

Ellis, R.A., Jacob, D.J., Sulprizio, M.P., Zhang, L., Holmes, C.D., Schichtel, B.A., Blett, Porter, E., Pardo, L.H., Lynch, J.A., 2013. Present and future nitrogen deposition to national parks in the United States: critical load exceedances. Atmospheric Chemistry and Physics, 13, 9083-9095.

Fahey, K.M. et al., 2017. A framework for expanding aqueous chemistry in the Community Multiscale Air Quality (CMAQ) model version 5.1. Geoscientific Model Development, 10, 1587.

Farmer, D.K., Cohen, R.C., 2008. Observations of HNO_3, ΣAN, ΣPN and NO_2 fluxes: evidence for rapid HOx chemistry within a pine forest canopy. Atmospheric Chemistry and Physics, 8, 3899–3917.

Flechard, C., Nemitz, E., Smith, R., Fowler, D., Vermeulen, A., Bleeker, A., et al. 2011. Dry deposition of reactive nitrogen to European ecosystems: A comparison of inferential models across the NitroEurope network. Atmospheric Chemistry and Physics, 11, 2703–2728.

Galloway, J.N., Townsend, A.R., Erisman, J.W., Bekunda, M., Cai, Z., Freney, J.R., Martinelli, L.A., Seitzinger, S.P., Sutton, M.A., 2008. Transformation of the nitrogen cycle: recent trends, questions and potential solutions. Science, 320, 889-892.

Giorgi, F., 1986. A particle dry deposition parameterization scheme for use in tracer transport models. Journal of Geophysical Research - Atmospheres, 91, 9794-9806.

Hansen, K., Sørensen, L.L., Hertel, O., Geels, C., Skjøth, C.A., Jensen, B., Boegh, E., 2013. Ammonia emissions from deciduous forest after leaf fall. Biogeosciences, 10, 4577–4589.

909   Hansen, K., Personne, E., Skjoth, C.A., Loubet, B., Ibrom, A., Jensen, R., Sorenson, L.L., Beogh, E., 2017.
910   Investigation sources of measured forest-atmospheric ammonia fluxes using tow-layer bi-directional modelling.
911   Agricultural and Forest Meteorology, 237-238, 80-94.

912   Harman, I.N., Finnigan, J.J., 2007. A simple unified theory for flow in the canopy and roughness sublayer. Boundary
913   Layer Meteorology, 123, 339-363.

914   Hicks, B.B., 2008. On estimating dry deposition rates in complex terrain. Journal of Applied Meteorology and
915   Climatology, 47, 1651 – 1658.

916   Hill, P.W., Raven, J.A., Sutton, M.A., 2002. Leaf age-related differences in apoplastic NH_4^+ concentration, pH and
917   the NH_3 compensation point for a wild perennial. Journal of Experimental Botany, 53, 277–286.

918   Holland, E.A., Dentener, F.J., Braswell, B.H., Sulzman, J.M. 1999. Contemporary and pre-industrial global reactive
919   nitrogen budgets. Biogeochemistry, 46, 7-43.

920   Husted, S., Schjoerring, J.K., 1995. Apoplastic pH and ammonium concentration in leaves of Brassica napus L. Plant
921   Physiology, 1453-1460.

922   Jickells, T., Baker, A.R., Cape, J.N., Cornell, S.E., Nemitz, E., 2013. The cycling of organic nitrogen through the
923   atmosphere. Philosophical Transactions of the Royal Society B 368, 20130115.

924   Keene, W.C., Montag, J.A., Maben, J.R., Southwell, M., Leonard, J., Church, T.M., Moody, J.L., Galloway, J.N.,
925   2002. Organic nitrogen in precipitation over Eastern North America. Atmospheric Environment, 36, 4529–4540.

926   Kim, P.S., Jacob, D.J., Fisher, J.A., Travis, K., Yu, K., Zhu, L., Yantosca, R.M., Sulprizio, M.P., Jimenez, J.L.,
927   Campuzano-Jost, P., Froyd, K.D., Liao, J., Hair, J.W., Fenn, M.A., Butler, C.F., Wagner, N.L., Gordon, T.D.,
928   Welti, A., Wennberg, P.O., Crounse, J.D., St. Clair, J.M., Teng, A.P., Millet, D.B., Schwarz, J.P., Markovic,
929   M.Z., and Perring, A.E., 2015 Sources, seasonality, and trends of southeast US aerosol: an integrated analysis of
930   surface, aircraft, and satellite observations with the GEOS-Chem chemical transport model, Atmospheric
931   Chemistry and Physics, 15, 10411–10433.

932   Knoepp, J.D., Vose, J.M, Swank, W.T., 2008. Nitrogen deposition and cycling across an elevation and vegetation
933   gradient in southern Appalachian forests. International Journal of Environmental Studies, 65, 389–408.

934   Knoepp, J.D., See, C.R., Vose, J.M., Miniat, C.F., Clark, J.S., 2018. Total C and N pools and fluxes vary with time,
935   soil temperature, and moisture along an elevation, precipitation, and vegetation gradient in southern Appalachian
936   forests. Ecosystems, 21, 1623–1638.

937   LaCount, M.D., Haeuber, R.A., Macy, T.R., Murray, B.A., 2021. Reducing power sector emissions under the 1990
938   Clean Air Act Amendments: A retrospective on 30 years of program development and implementation.
939   Atmospheric Environment, 245, 118012.

940   Laseter, S.H., Ford, C.R., Vose, J.M., Swift, L.W. Jr., 2012. Long-term temperature and precipitation trends at the
941   Coweeta Hydrologic Laboratory, Otto, North Carolina, USA. Hydrology Research, 43, 890-901.

942   Lavery, T.F., Rogers, C.M., Baumgardner, R., Mishoe, K.P., 2009. Intercomparison of Clean Air Status and Trends
943   Network nitrate and nitric acid measurements with data from other monitoring programs. Journal of the Air &
944   Waste Management Association, 59, 214-226.

945 Lee, H.-M., Paulot, F., Henze, D. K., Travis, K., Jacob, D. J., Pardo, L. H., Schichtel, B. A. 2016 Sources of nitrogen
946   deposition in Federal Class I areas in the US, Atmospheric Chemistry and Physics, 16, 525-540.

947 Lehner, M., Rotach, M.W., 2018. Current challenges in understanding and predicting transport and exchange in the
948   atmosphere over mountainous terrain. Atmosphere, 9, 276.

949 Li, Y., Schichtel, B.A., Walker, J.T., Schwede, D.B., Chen, X., Lehmann, C.M.B., Puchalski, M.A., Gay, D.A.,
950   Collett, J.L., 2016. Increasing importance of deposition of reduced nitrogen in the United States. Proceedings of
951   the National Academy of Sciences, 113, 5874-5879.

952 Lin, M., Walker, J., Geron, C., Khlystov, A., 2010. Organic nitrogen in PM2.5 aerosol at a forest site in the Southeast
953   US. Atmospheric Chemistry and Physics, 10, 2145–2157.

954 Lohse, K.A., Hope, D., Sponseller, R., Allen, J.O., Grimm, N.B., 2008. Atmospheric deposition of carbon and
955   nutrients across an arid metropolitan area. Science of the Total Environment, 402, 95-105.

956 Lynch, J.A., Phelan, J., Pardo L.H., McDonnell, T.C., Clark, C.M., 2017. Detailed Documentation of the National
957   Critical Load Database (NCLD) for U.S. Critical Loads of Sulfur and Nitrogen, version 3.0. National Atmospheric
958   Deposition Program, Illinois State Water Survey, Champaign, IL.

959 Makar, P.A., Akingunola, A., Aherne, J., Cole, A.S., Aklilu, Y.-A., Zhang, J., Wong, I., Hayden, K., Li, S.-M., Kirk,
960   J., Scott, K., Moran, M.D., Robichaud, A., Cathcart, H., Baratzedah, P., Pabla, B., Cheung, P., Zheng, Q., Jeffries,
961   D.S., 2018. Estimates of exceedances of critical loads for acidifying deposition in Alberta and Saskatchewan.
962   Atmospheric Chemistry and Physics, 18, 9897-9927.

963 Massad, R.-S., Nemitz, E., Sutton, M., 2010. Review and parameterisation of bi-directional ammonia exchange
964   between vegetation and the atmosphere. Atmospheric Chemistry and Physics, 10, 10359-10386.

965 Mattsson, M., Schjoerring, J.K., 2002. Dynamic and steady-state responses of inorganic nitrogen pools and NH_3
966   exchange in leaves of Lolium perenne and Bromus erectus to changes in root nitrogen supply. Plant Physiology,
967   128, 742–750.

968 Mattsson, M., Herrmann, B., Jones, S., Neftel, A., Sutton, M.A., Schjoerring, J.K., 2009. Contribution of different
969   grass species to plant-atmosphere ammonia exchange in intensively managed grassland. Biogeosciences, 6, 59–
970   66.

971 McDonnell, T.C., Reinds, G.J., Sullivan, T.J., Clark, C.M., Bonten, L.T.C., Mol-Dijkstra, J.P., Wamelink, G.W.W.,
972   Dovciak, M., 2018. Feasibility of coupled empirical and dynamic modeling to assess climate change and air
973   pollution impacts on temperate forest vegetation of the eastern United States. Environmental Pollution, 234, 902-
974   914.

975 McNulty, S.G., Cohen, E.C., Myers, J.A.M., Sullivan, T.J., Li, H., 2007. Estimates of critical acid loads and
976   exceedances for forest soils across the conterminous United States. Environmental Pollution 149, 281–292.

977 NPS, 2020. National Park Service. Clean Air Status and Trends Network, hourly trace gas data, available at
978   www.epa.gov/castnet. Accessed 06/11/2020.

979 Meyers, T.P., Hall, M.E., Lindberg, S.E., Kim, K., 1996. Use of the modified Bowen-ratio technique to measure fluxes
980   of trace gases. Atmospheric Environment, 30, 3321 – 3329.

981 Neff, J.C., Holland, E.A., Dentener, F.J., Mcdowell, W.H., Russell, K.M., 2002a. The origin, composition and rates
982   of organic nitrogen depiction: A missing piece of the nitrogen cycle? Biogeochemistry, 57/58, 99-136.

983 Neff, J.C., Townsend, A.R., Gleixner, G., Lehman, S.J., Turnbull, J., Bowman, W., 2002b. Variable effects of nitrogen
984   additions on the stability and turnover of soil carbon. Nature 419, 915-917.

985 Nemitz, E., Sutton, M., Gut, A., San Jose, R., Husted, S., Schjoerring, J., 2000a. Sources and sinks of ammonia within
986   an oilseed rape canopy. Agricultural and Forest Meteorology, 105, 385–404.

987 Nemitz, E., Sutton, M.A., Schjoerring, J.K., Husted, S., Wyers, G.P., 2000b. Resistance modelling of ammonia
988   exchange over oilseed rape. Agricultural and Forest Meteorology, 10, 405-425.

989 Nemitz, E., Milford, C., Sutton, M.A., 2001. A two-layer canopy compensation point model for describing bi-
990   directional biosphere-atmosphere exchange of ammonia. Quarterly Journal of the Royal Meteorological Society,
991   127, 815-833.

992 Nemitz, E., Sutton, M.A., Wyers, G.P., Jongejan, P.A.C., 2004a. Gas-particle interactions above a Dutch heathland:
993   I. Surface exchange fluxes of NH_3, SO_2, HNO_3 and HCl. Atmospheric Chemistry and Physics, 4, 989-1005.

994 Nemitz, E., Sutton, M.A., Wyers, G.P., Otjes, R.P., Mennen, M.G., van Putten, E.M., Gallagher, M.W., 2004b. Gas-
995   particle interactions above a Dutch heathland: II. Concentrations and surface exchange fluxes of atmospheric
996   particles. Atmospheric Chemistry and Physics, 4, 1007 – 1024.

997 Nilsson, J., Greenfelt, P., 1988. Critical levels for sulphur and nitrogen, 418 pp., Nordic Council of Ministers,
998   Copenhagen, Denmark.

999 Nouaime, G., Bertman, S.B., Seaver, C., Elyea, D., Huang, H., Shepson, P. B., Starn, T. K., Riemer, D. D., Zika, R.
1000   G., Olszyna, K., 2012. Sequential oxidation products from tropospheric isoprene chemistry: MACR and MPAN
1001   at a NOx -rich forest environment in the southeastern United States. Journal of Geophysical Research -
1002   Atmospheres, 103, 22463–22471.

1003 Novick, K.A, Walker, J.T., Chan, W.S., Sobek, C., Vose, J., 2013. Eddy covariance measurements with a new fast-
1004   response, closed-path analyzer: spectral characteristics and cross-system comparisons. Agricultural and Forest
1005   Meteorology, 181, 17-32.

1006 Novick, K., Brantley, S., Ford Miniat, C., Walker, J.T., Vose, J., 2014. Inferring the contribution of advection to total
1007   ecosystem scalar fluxes over a tall forest in complex terrain. Agricultural and Forest Meteorology, 185, 1-13.

1008 Novick, K.A., Oishi, A.C., Miniat, C.F., 2016. Cold air drainage flows subsidize montane valley ecosystem
1009   productivity. Global Change Biology, 22, 4041-4027.

1010 Oishi, A.C., Miniat, C.F., Novick, K.A., Brantley, S.T., Vose, J.M., Walker, J.T., 2018. Warmer temperatures reduce
1011   net carbon uptake, but not water use in a mature southern Appalachian forest. Agricultural and Forest
1012   Meteorology, 252, 269-282.

1013 Ollinger, S.V., Aber, J.D., Reich, P.B., Freuder, R.J., 2002. Interactive effects of nitrogen deposition, tropospheric
1014   ozone, elevated CO_2 and land use history on the carbon dynamics of northern hardwood forests. Global Change
1015   Biology, 8, 545-562.

1016 Pardo, L.H., Fenn, M.E., Goodale, C.L., Geiser, L.H.,Driscoll, C.T., Allen, E.B., Baron, J.S., Bobbink, R., Bowman,
1017   W.D., Clark, C.M., Emmett, B., Gilliam, F.S., Greaver, T.L., Hall, S.J., Lilleskov, E.A., Liu, L., Lynch, J.A.,

1018   Nadelhoffer, K.J., Perakis, S.S., Robin-Abbott, M.J., Stoddard, J.L., Weathers, K.C., Dennis, R.L., 2011. Effects
1019   of nitrogen deposition and empirical nitrogen critical loads for ecoregions of the United States. Ecological
1020   Applications 21, 3049-3082.

1021   Pardo, LH., Duarte, N., Van Miegroet, H., Fisher, L.S, Robin-Abbott, M.J., 2018. Critical loads of sulfur and nitrogen
1022   and modeled effects of deposition reduction for forested ecosystems of Great Smoky Mountains National Park.
1023   Gen. Tech. Rep. NRS-180. Newtown Square, PA: U.S. Department of Agriculture, Forest Service, Northern
1024   Research Station. 26 p. https://doi.org/10.2737/NRS-GTR-180.

1025   Paulot, F., Henze, D.K., Wennberg, P.O., 2012. Impact of the isoprene photochemical cascade on tropical ozone,
1026   Atmospheric Chemistry and Physics, 12, 1307–1325.

1027   Paulot, F., Jacob, D.J., 2014. Hidden cost of U.S. agricultural exports: particulate matter from ammonia emissions.
1028   Environmental Science and Technology, 48, 903-908.

1029   Pearson J., Woodall J., Clough E.C.M., Nielsen K.H., Schjoerring, J.K., 2002. Production and consumption of NH_3 in
1030   trees. In: Gasche R, Papen H, Rennenberg H (eds) Trace gas exchange in forest ecosystems. Kluwer Academic,
1031   The Netherlands, pp 53–77.

1032   Personne, E., Tardy, F., Genermont, S., Decuq, C., Gueudet, J.-C., Mascher, N., Durand, B., Masson, S., Lauransot,
1033   M., Flechard, C., Burkhardt, J., Loubet, B., 2015. Investigating sources and sinks for ammonia exchanges between
1034   the atmosphere and a wheat canopy following slurry application with trailing hose. Agricultural and Forest
1035   Meteorology, 207, 11-23.

1036   Pleim, J., Ran, L., 2011. Surface flux modeling for air quality applications. Atmosphere, 2, 271-302.

1037   Pleim, J.E., Xiu, A., 1995. Development and testing of a surface flux and planetary boundary layer model for
1038   application in mesoscale models. Journal of Applied Meteorology, 34, 16-32.

1039   Poorter, H., Niinemets, Ü, Poorter, L., Wright, I.J., Villar, R., 2009. Causes and consequences of variation in leaf mass
1040   per area (LMA): a meta-analysis. New Phytologist, 182, 565-588.

1041   Nanus, L., McMurray, J.A., Clow, D.W., Saros, J.E., Blett, T., Gurdak, J.J., 2017 Spatial variation of atmospheric
1042   nitrogen deposition and critical loads for aquatic ecosystems in the Greater Yellowstone Area. Environmental
1043   Pollution, 223, 644-656.

1044   Root, H.T., Geiser, L.H., Jovan, S., Neitlich, P., 2015. Epiphytic macrolichen indication of air quality and climate in
1045   interior forested mountains of the Pacific Northwest, USA. Ecological Indicators, 53, 95–105.

1046   Rumsey, I., Cowen, K., Walker, J.T., Kelley, T.J., Hanft, E.A., Mishoe, K., Rogers, C., Proost, R., Beachley, G.M.,
1047   Lear, G., Frelink, T., Otjes, R.P., 2014. An assessment of the performance of the Monitor for AeRosols and GAses
1048   in ambient air (MARGA): a semi-continuous method for soluble compounds. Atmospheric Chemistry and
1049   Physics, 14, 5639–5658.

1050   Samy, S., Robinson, J., Rumsey, I.C., Walker, J.T., Hays, M.D., 2013. Speciation and trends of organic nitrogen in
1051   southeastern U.S. fine particulate matter ($PM_{2.5}$). Journal of Geophysical Research, 118, 1996-2006.

1052   Schneider S., Geβler A., Weber P., von Sengbusch D., Hanemann U., Rennenberg H., 1996. Soluble N compounds in
1053   trees exposed high loads of N: a comparison of spruce (*Picea abis*) and beech (*Fagus sylvatica*) grown under field
1054   conditions. New Phytologist, 134, 103–114.

1055   Schwede, D.B., Lear, G.G., 2014. A novel hybrid approach for estimating total deposition in the United States.
1056   Atmospheric Environment, 92, 207-220.

1057   Scudlark, J.R., Russell, K.M., Galloway, J.N., Church, T.M., Keene, W.C., 1998. Organic nitrogen in precipitation at
1058   the mid-Atlantic US coast - Methods evaluation and preliminary measurements. Atmospheric Environment, 32,
1059   1719–1728.

1060   Shuttleworth, W.J., Wallace, J.S., 1985. Evaporation from sparse crops – an energy combination theory. Quarterly
1061   Journal of the Royal Meteorological Society, 11, 839-855.

1062   Sickles II, J.E., Shadwick, D.S., 2015. Air quality and atmospheric deposition in the eastern US: 20 years of change,
1063   Atmospheric Chemistry and Physics, 15, 173–197.

1064   Slinn, W.G.N., 1982. Predictions for particle deposition to vegetative surfaces. Atmospheric Environment, 16, 1785-
1065   1794.

1066   Simkin, S.M., Allen, E.B., Bowman, W.D., Clark, C.M., Belnap, J., Brooks, M.L., Cade, B.S., Collins, S.L., Geiser,
1067   L.H., Gilliam, F.S., Jovan, S.E., Pardo, L.H., Schulz, B.K., Stevens, C.J., Suding, K.N., Throop, H.L., and Waller,
1068   D.M., 2016. Conditional vulnerability of plant diversity to atmospheric nitrogen deposition across the United
1069   States. Proceedings of the National Academy of Sciences, 113, 4086-4091.

1070   Sutton, M.A., Asman, W.A.H., Ellermann, T., Van Jaarsveld, J.A., Acker, K., Aneja, V., Duyzer, J., Horvath, L.,
1071   Paramonov, S., Mitosinkova, M., Tang, Y.S., Achermann, B., Gauger, T., Bartniki, J., Neftel, A., Erisman, J.W.,
1072   2003. Establishing the link between ammonia emission control and measurements of reduced nitrogen
1073   concentrations and deposition. Environmental Monitoring and Assessment, 82, 149–185.

1074   Sutton, M.A., Nemitz, E., Milford, C., Campbell, C., Erisman, J.W., Hensen, A., Cellier, P., David, M., Loubet, B.,
1075   Personne, E., Schjoerring, J.K., Mattsson, M., Dorsey, J.R., Gallagher, M.W., Horvath, L., Weidinger, T.,
1076   Meszaros, R., Dämmgen, U., Neftel, A., Herrmann, B., Lehman, B.E., Flechard, C., Burkhardt, J., 2009.
1077   Dynamics of ammonia exchange with cut grassland: synthesis of results and conclusions of the GRAMINAE
1078   Integrated Experiment. Biogeosciences, 6, 2907–2934.

1079   Tang, Y.S., Cape, J.N., Sutton, M.A., 2001. Development and types of passive samplers for monitoring atmospheric
1080 NO_2 and NH_3 concentrations. The Scientific World, 1, 513–529.

1081   Toma, S., Bertman, S., Groff, C., Xiong, F., Shepson, P.B., Romer, P., Duffey, K., Wooldridge, P., Cohen, R.,
1082   Baumann, K., Edgerton, E., Koss, A. R., de Gouw, J., Goldstein, A., Hu, W., Jimenez, J.L., 2019. Importance of
1083   biogenic volatile organic compounds to acyl peroxy nitrates (APN) production in the southeastern US during
1084   SOAS 2013, Atmospheric Chemistry and Physics, 19, 1867–1880.

1085   Trainer, M., Parrish, D.D., Buhr, M.P., Norton, R.B., Fehsenfeld, F.C., Anlauf, K.G., Bottenheim, J.W., Tang, Y.Z.,
1086   Wiebe, H.A., Roberts, J.M., Tanner, R.L., Newman, L., Bowersox, V.C., Meagher, J.F., Olszyna, K.J., Rodgers,
1087   M.O., Wang, T., Berresheim, H., Demerjian, K.L., Roychowdhury, U.K., 1993. Correlation of ozone with NOy
1088   in photochemically aged air. Journal of Geophysical Research - Atmospheres, 98, 2917–2925.

1089   U.S. EPA, 2014. U.S. Environmental Protection Agency, 2014. Data from the 2014 National Emissions Inventory,
1090   Version 2. Retrieved 2018 from https://www.epa.gov/air-emissions inventories/2014-national-emissions-
1091   inventory-nei-data

U.S. EPA, 2019a. U.S. Environmental Protection Agency Critical Loads Mapper Tool https://www.epa.gov/air-research/critical-loads-mapper-tool.

U.S. EPA. 2019b. Integrated Science Assessment (ISA) for Oxides of Nitrogen, Oxides of Sulfur and Particulate Matter Ecological Criteria (Final Report). U.S. Environmental Protection Agency, Washington, DC, EPA/600/R-20/278.

van Houtven, G., Phelan, J., Clark, C., Sabo, R.D., Buckley, J., Thomas, R.Q., et al., 2019. Nitrogen deposition and climate change effects on tree species composition and ecosystem services for a forest cohort. Ecological Monographs, 89, e01345.

Walker, J.T., Dombek, T.L., Green,L.A., Gartman,N., Lehmann, C.M.B., 2012. Stability of organic nitrogen in NADP wet deposition samples. Atmospheric Environment, 60, 573-582.

Walker, J.T., Bell, M.D., Schwede, D., Cole, A., Beachley, G., Lear, G., Wu, Z., 2019a. Aspects of uncertainty in total reactive nitrogen deposition estimates for North American critical load applications. Science of the Total Environment, 690, 1005-1018.

Walker, J.T., Beachley, G., Amos, H.M., Baron, J.S., Bash, J., et al. 2019b. Toward the improvement of total nitrogen deposition budgets in the United States. Science of the Total Environment, 691, 1328-1352.

Walker, J.T., Beachley, G., Zhang, L.,Benedict, K.B., Sive, B.C., Schwede, D.B., 2020. A review of measurements of air-surface exchange of reactive nitrogen in natural ecosystems across North America, Science of the Total Environment, 698, 133975.

Wang, L., Xu, Y., Schjoerring, J.K., 2011. Seasonal variation in ammonia compensation point and nitrogen pools in beech leaves (*Fagus sylvatica*). Plant Soil, 343, 51–66.

Weathers, K.C., Simkin, S.M., Lovett, G.M., Lindberg, S.E., 2006. Empirical modeling of atmospheric deposition in mountainous landscapes. Ecological Applications, 16, 1590-1607.

Wentworth, G.R., Murphy, J.G., Benedict, K.B., Bangs, E.J., Collett Jr., J.L., 2016. The role of dew as a night-time reservoir and morning source for atmospheric ammonia. Atmospheric Chemistry and Physics, 16, 7435–7449.

Whitall, D.R., Paerl, H.W., 2001. Spatiotemporal variability of wet atmospheric nitrogen deposition to the Neuse River Estuary, North Carolina. Journal of Environmental Quality, 30, 1508–1515.

Williams, E.J., Baumann, K., Roberts, J.M., Bertman, S.B., Norton, R.B., Fehsenfeld, F.C., Springston, S.R., Nunnermacker, L.G., Newman, L., Olszyna, K, Meagher, J., Hartsell, B., Edgerton, E., Pearson, J.R., Rodgers, M.O., 1998. Intercomparison of ground-based NOy measurements techniques. Journal of Geophysical Research - Atmospheres, 103, 22261-22280.

Wolfe, G.M., Thornton, J.A., Yatavelli, R.L.N., McKay, M., Goldstein, A.H., LaFranchi, B., Min, K.-E., Cohen, R.C., 2009. Eddy covariance fluxes of acyl peroxy nitrates (PAN, PPN and MPAN) above a Ponderosa pine forest. Atmospheric Chemistry and Physics, 9, 615–634.

Xing, J., Pleim, J., Mathur, R., Pouliot, G., Hogrefe, C., Gan, C.-M., Wei, C., 2013. Historical gaseous and primary aerosol emissions in the United States from 1990 to 2010. Atmospheric Chemistry and Physics, 13, 7531–7549.

Yao, X., Zhang, L. 2019. Causes of large increases in atmospheric ammonia in the last ecade across North America. ACS Omega, 4, 22133-22142.

1129 Yi, C., 2008. Momentum transfer within canopies. Journal of Applied Climatology, 47, 262-275

1130 Yu, F., Nair, A.A., Luo, G., 2018. Long-term trend of gaseous ammonia over the United States: Modeling and
1131   comparison with observations. Journal of Geophysical Research - Atmospheres, 123, 8315–8325.

1132 Zhang, L., Vet, R., Wiebe, A., Mihele, C., Sukloff, B., Chan, E., Moran, M.D., Iqbal., S., 2008. Characterization of
1133   the size-segregated water-soluble inorganic ions at eight Canadian rural sites. Atmospheric Chemistry and
1134   Physics, 8, 7133-7151.

1135 Zhang, R., Thompson, T.M., Barna, M.G., Hand, J.L., McMurray, J.A., Bell, M.D., Malm, W.C., Schichtel, B.A.
1136   2018. Source regions contributing to excess reactive nitrogen deposition in the Greater Yellowstone Area (GYA)
1137   of the United States. Atmospheric Chemistry and Physics, 18, 12991-13011.

1138
1139
1140
1141
1142
1143
1144
1145
1146
1147
1148
1149
1150
1151
1152
1153
1154
1155
1156
1157
1158

1159 **Tables and Figures**

1160

1161 Table 1. Sampling locations and type of sampler deployed.

Site code	Latitude(N)	Longitude(W)	Elevation(m)	Sampler type
NC25/COW137	35.0605	83.4305	686	AMoN (NC25), CASTNET (COW137), Tisch $PM_{2.5}$[*], DD-CL, TD-PC-CL, NTN (NC25), EPA precipitation
EFT[a]	35.0591	83.4274	690	MARGA[*], URG[*], Passive NH_3 and HNO_3, micrometeorology
WS18	35.0512	83.4337	806	Passive NH_3 and HNO_3
SK[b]	35.0482	83.4542	986	Passive NH_3 and HNO_3, CASTNET (COW005)
CS28	35.0466	83.4650	1189	Passive NH_3 and HNO_3
CS77	35.0303	83.4604	1425	Passive NH_3 and HNO_3

1162 [a]-Eddy flux tower; [b]-Screwdriver Knob; [*] Tisch $PM_{2.5}$, MARGA, and URG denuder/filter pack

1163 samplers were deployed only during intensive sampling periods.

1164 Table 2. Details of intensive and long-term atmospheric measurements at Coweeta.

Sampler name	Operating periods	Measured species	Resolution	Height(m)*
DD-CL, TD-PC-CL	August 2015-August 2016	HNO_3, NO_y, ΣAN^1, ΣPN^2	Hourly	8
MARGA	Spring, summer 2016 intensives	HNO_3, NH_3, NO_3^-, SO_4^{2-}, NH_4^+	Hourly	~40
URG denuder/filter	All intensives 2015-2016	HNO_3, NH_3, NO_2^-, NO_3^-, SO_4^{2-}, NH_4^+	3 or 4-hour integrated	~40
Tisch $PM_{2.5}$	All intensives 2015-2016	NO_2^-, NO_3^-, SO_4^{2-}, NH_4^+, WSTN	24hr integrated	~1
CASTNET (COW137)	Long-term	HNO_3, NO_3^-, SO_4^{2-}, NH_4^+, Cl^-, base cations	Weekly integrated	10
AMoN (NC25)	Long-term	NH_3	Bi-weekly passive	10
Passive HNO_3, NH_3	2015	HNO_3, NH_3	Bi-weekly	10
CASTNET (COW005)	2015	HNO_3, NO_3^-, SO_4^{2-}, NH_4^+, Cl^-, base cations	Weekly integrated	10
NADP/NTN	Long-term	NO_3^-, NH_4^+, SO_4^{2-}, Cl^-, H^+, base cations	Weekly accumulated	Ground
EPA precipitation	February 2015-August 2016	NO_2^-, NO_3^-, SO_4^{2-}, NH_4^+, WSTN	Weekly accumulated	Ground

1165 *Above ground; [1]Total alkylnitrates; [2]Total peroxynitrates

1166   Table 3. Summary of air concentration data sources for STAGE dry deposition modeling.

Chemical Species	Data Source	Details
NH_3	Measurement	AMoN measurement with diurnal profile imposed
HNO_3	Measurement	Continuous DD-CL
ΣPN	Measurement	Continuous TD-PC-CL. Assume molecular weight (MW = 121.1) of PAN ($C_2H_3NO_5$)
ΣAN	Measurement	Continuous TD-PC-CL. Assume molecular weight (MW = 135.1) of nitrooxy-butanol ($C_4H_9NO_4$)
NH_4^+	Measurement	CASTNET
NO_3^-	Measurement	CASTNET
PON	Estimated based on measured $NH_4^+ + NO_3^+$	Based on intensive direct measurements, assume PON represents 12% of total PON + NH_4^+ + NO_3^+
NO_2	Estimated based on measured NO_y	Based on ratio of NO_2/NO_y simulated by CMAQ V5.2.1 at Coweeta

1167
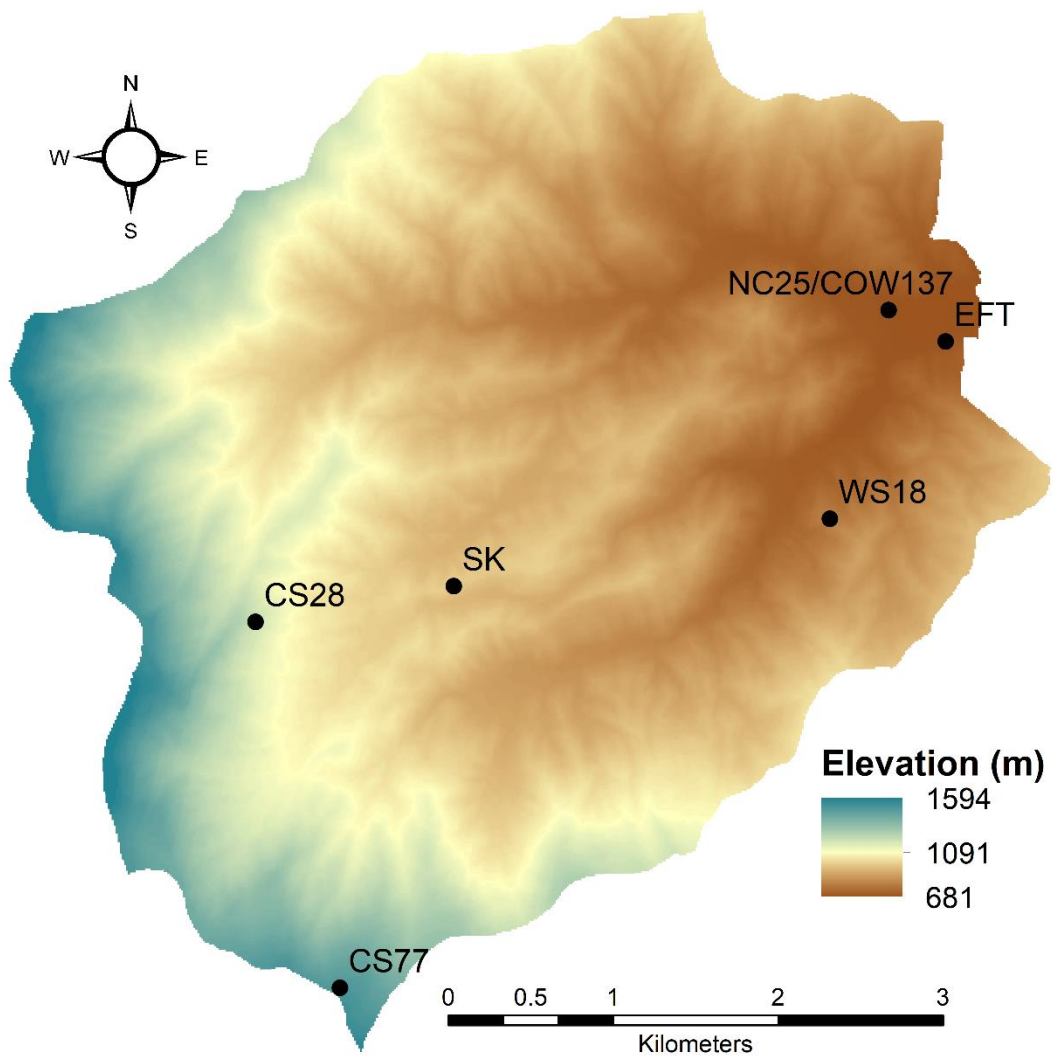
1170

Figure 1. Elevation map of Coweeta Basin with sampling sites in Table 1 indicated.
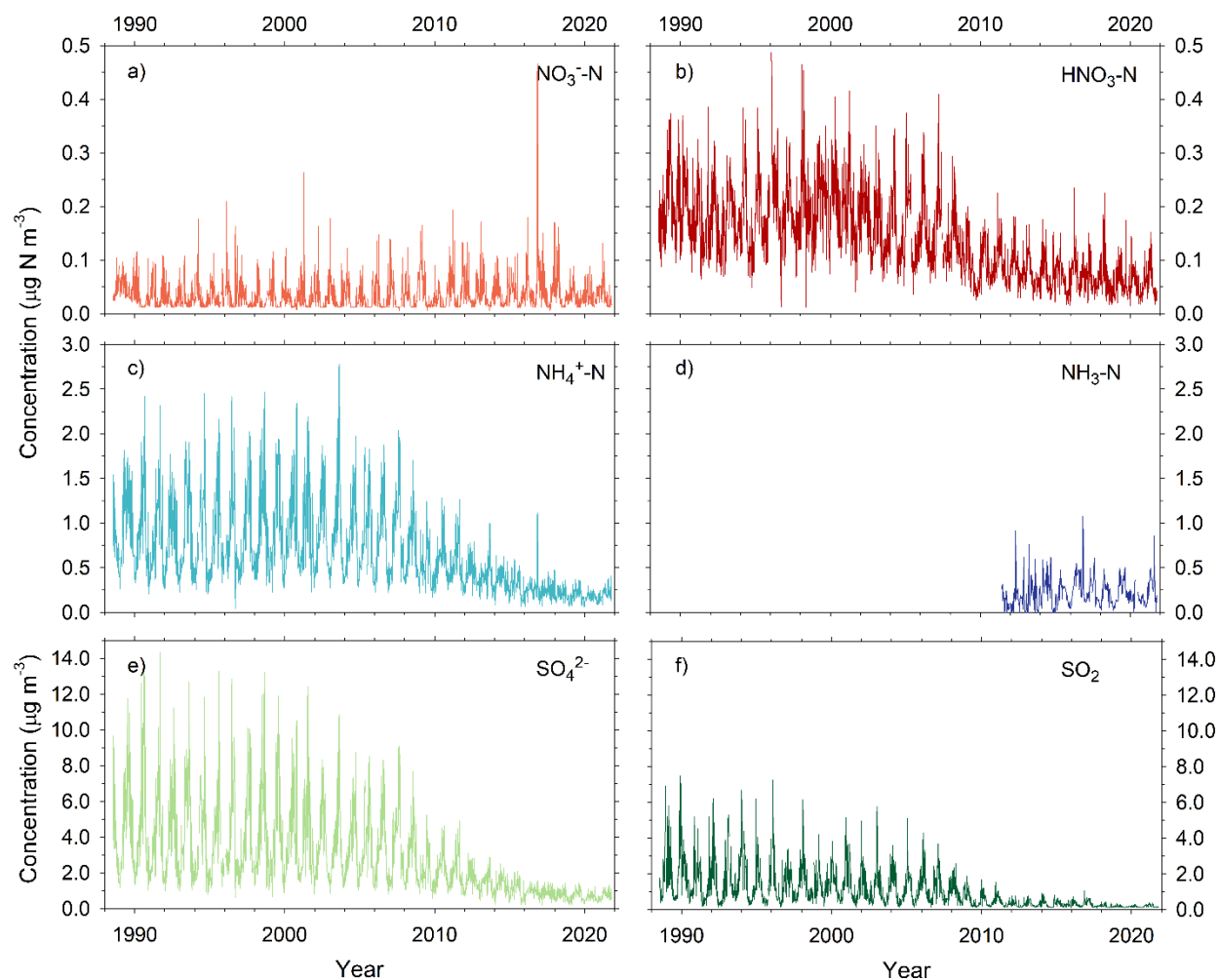
Figure 2. Long-term CASTNET (weekly, Site COW137) and AMoN (biweekly, Site NC25) air

1175   concentrations (as N) of NO_3^- (a), HNO_3 (b), NH_4^+ (c), NH_3 (d), SO_4^{2-} (e), and SO_2 (f).
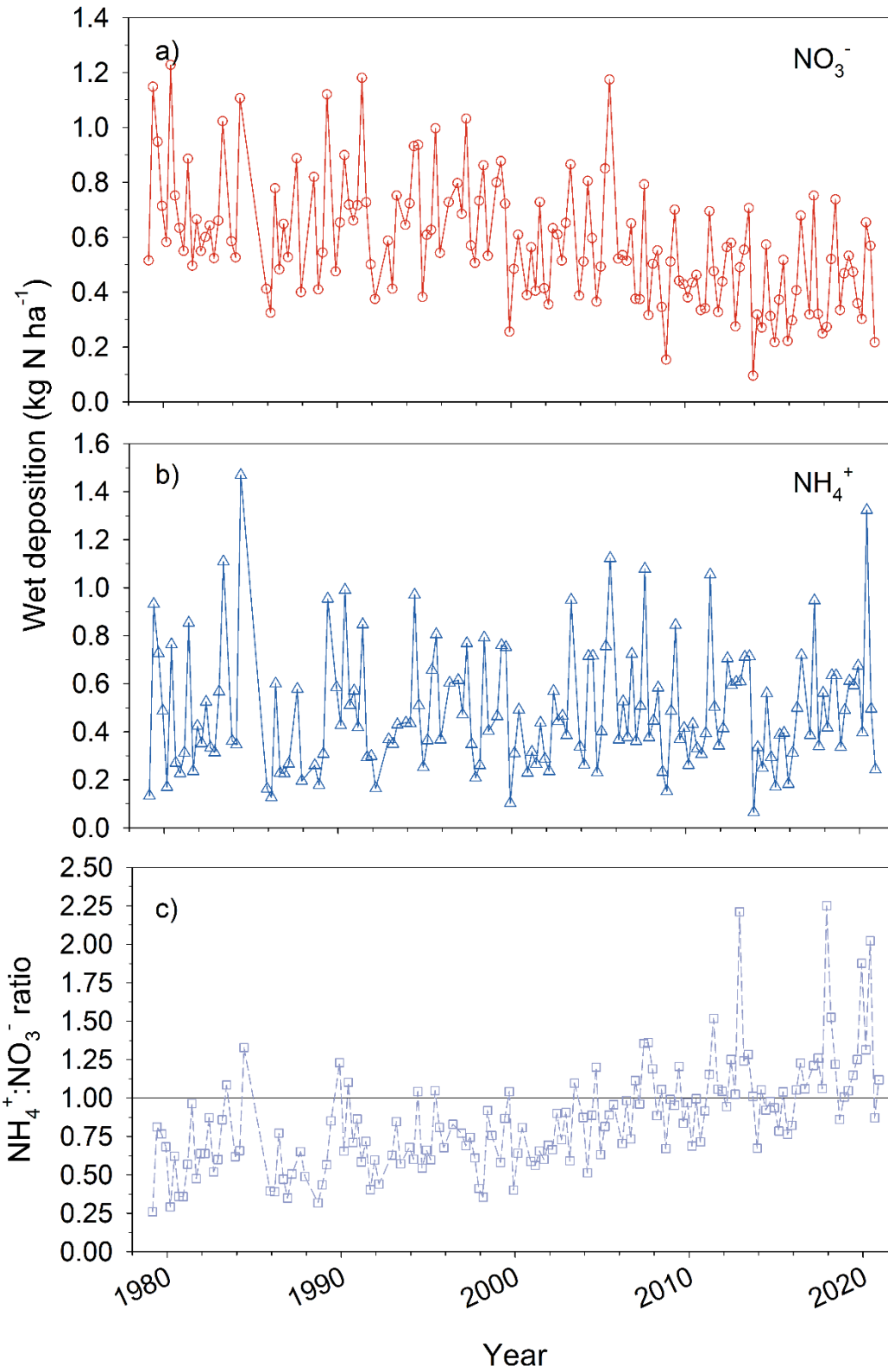
Figure 3. Long-term NTN NC25 measurements of seasonal NH_4^+ (a) and NO_3^- (b) wet deposition along with the ratio of NH_4^+ to NO_3^- as nitrogen and 1:1 reference line (c).
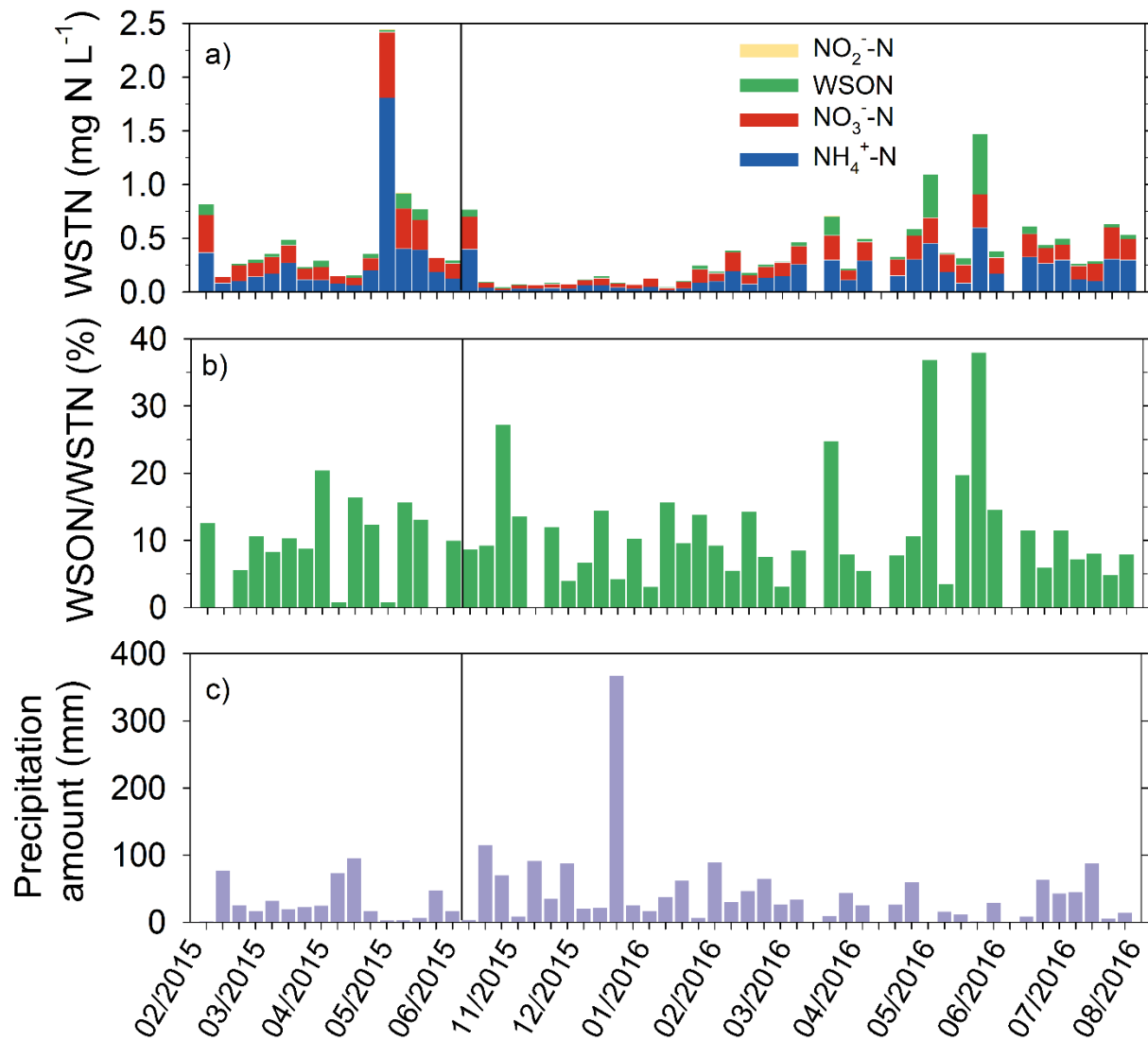
1180

Figure 4. Concentrations of nitrogen species in weekly precipitation samples (a), percentage contribution of WSON to WSTN in precipitation (b), and precipitation amount (c). Vertical line marks discontinuity due to missing data from 06/01/2015 to 10/19/2015.
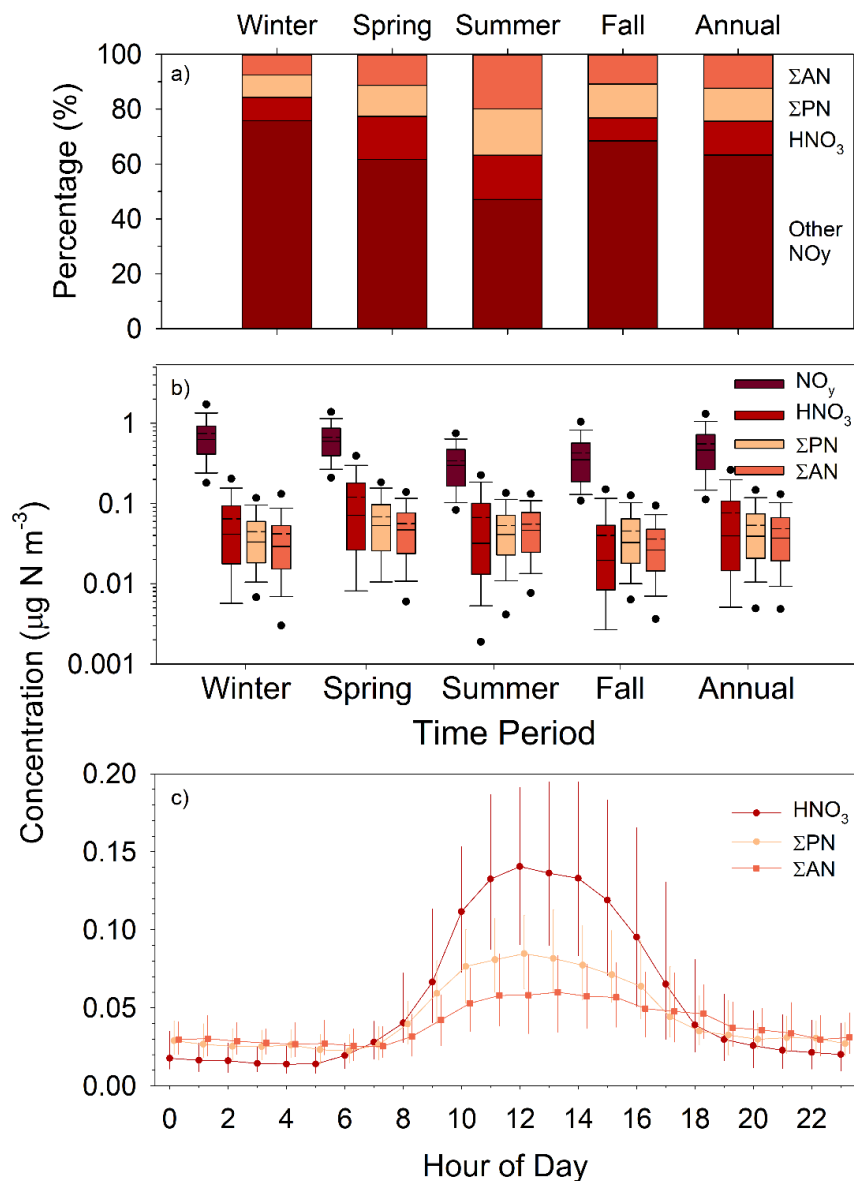
1185

Figure 5. Seasonal and annual % contribution of HNO_3, ΣPN, ΣAN, and other compounds to total Noy (a); seasonal and annual boxplots of NO_y, HNO_3, ΣPN and ΣAN where solid and dashed lines inside box represent median and mean, respectively; top and bottom of box represent 75th and 25th percentiles; whiskers represent 10th and 90th percentiles, and dots represent 5th and 95th percentiles

1190 (b); and diurnal profiles of HNO_3, ΣPN, and ΣAN where observations represent median hourly concentration and bars represent interquartile range (c). "Other NOy" is calculated as $NO_y - HNO_3 - \Sigma PN - \Sigma AN$ which, while primarily comprised of NO_x, includes N_2O_5, HONO, NO_3^-, and possibly other organics.
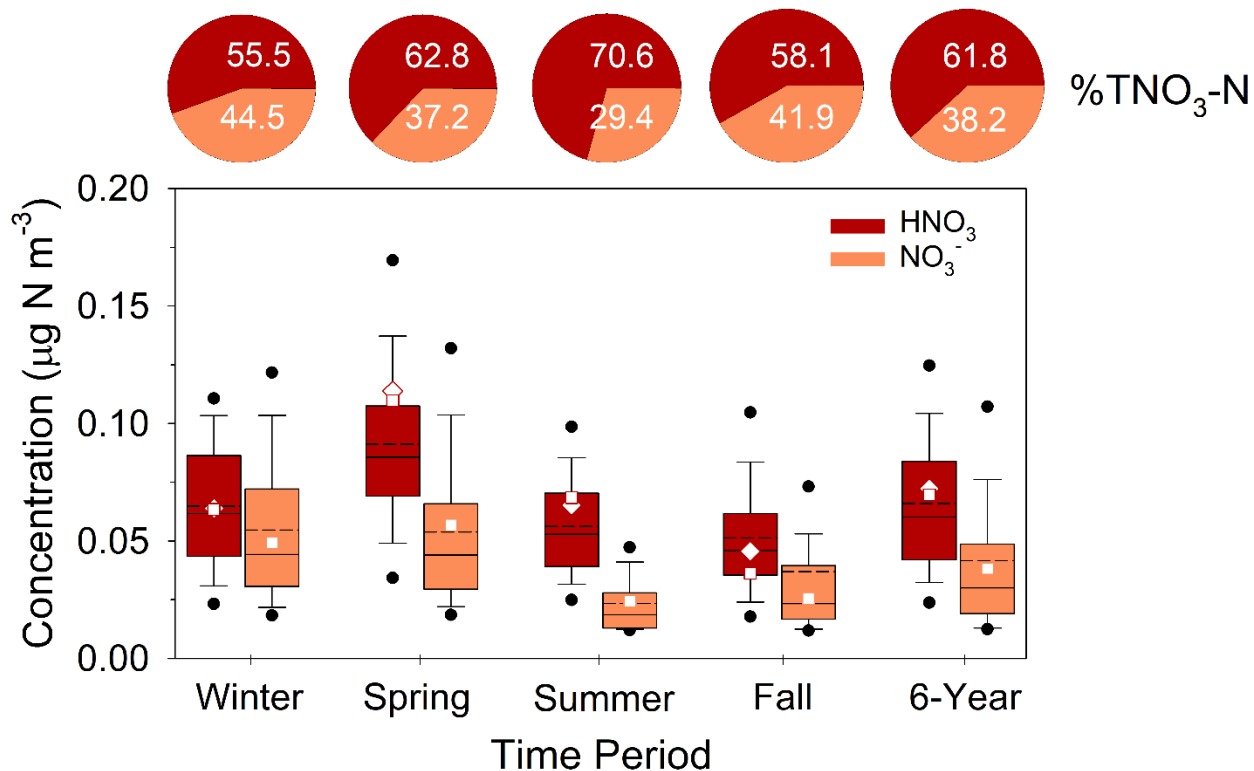
Figure 6. Summary of CASTNET HNO_3 and NO_3^- concentrations (as N) from 2015-2020 during winter, spring, summer and fall. Solid and dashed lines inside box represent median and mean, respectively. Top and bottom of box represent 75th and 25th percentiles. Whiskers represent 10th and 90th percentiles and dots represent 5th and 95th percentiles. "6-Year" represents the statistics for the entire 6-Year period. Squares and diamonds represent the seasonal and annual mean CASTNET (HNO_3 and NO_3^-) and continuous DD-CL HNO_3 for the August 2015 – August 2016 modeling period, respectively. Pie charts represent average % contribution of HNO_3 and NO_3^- to total NO_3^- ($HNO_3 + NO_3^-$) expressed as nitrogen.
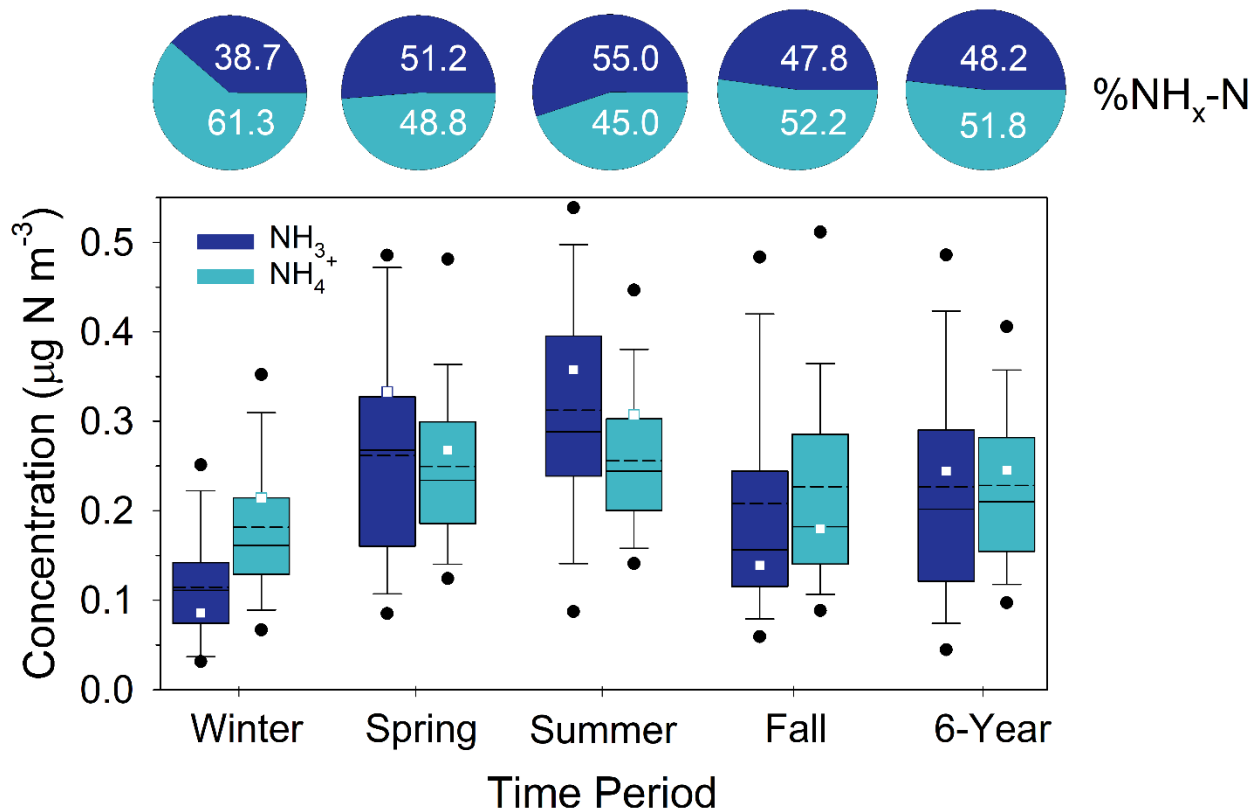
Figure 7. Summary of AMoN NH_3 and CASTNET NH_4^+ concentrations (as N) from 2015-2020 during winter, spring, summer and fall. Solid and dashed lines inside box represent median and mean, respectively. Top and bottom of box represent 75th and 25th percentiles. Whiskers represent 10th and 90th percentiles and dots represent 5th and 95th percentiles. "6-Year" represents the statistics for the entire 6-Year period. Squares represent the seasonal and annual mean concentration for the August 2015 – August 2016 modeling period. Pie charts represent average % contribution of NH_3 and NH_4^+ to total NH_x ($NH_3+NH_4^+$) expressed as nitrogen. AMoN concentrations were adjusted by subtracting the mean travel blank for the 6-year period.
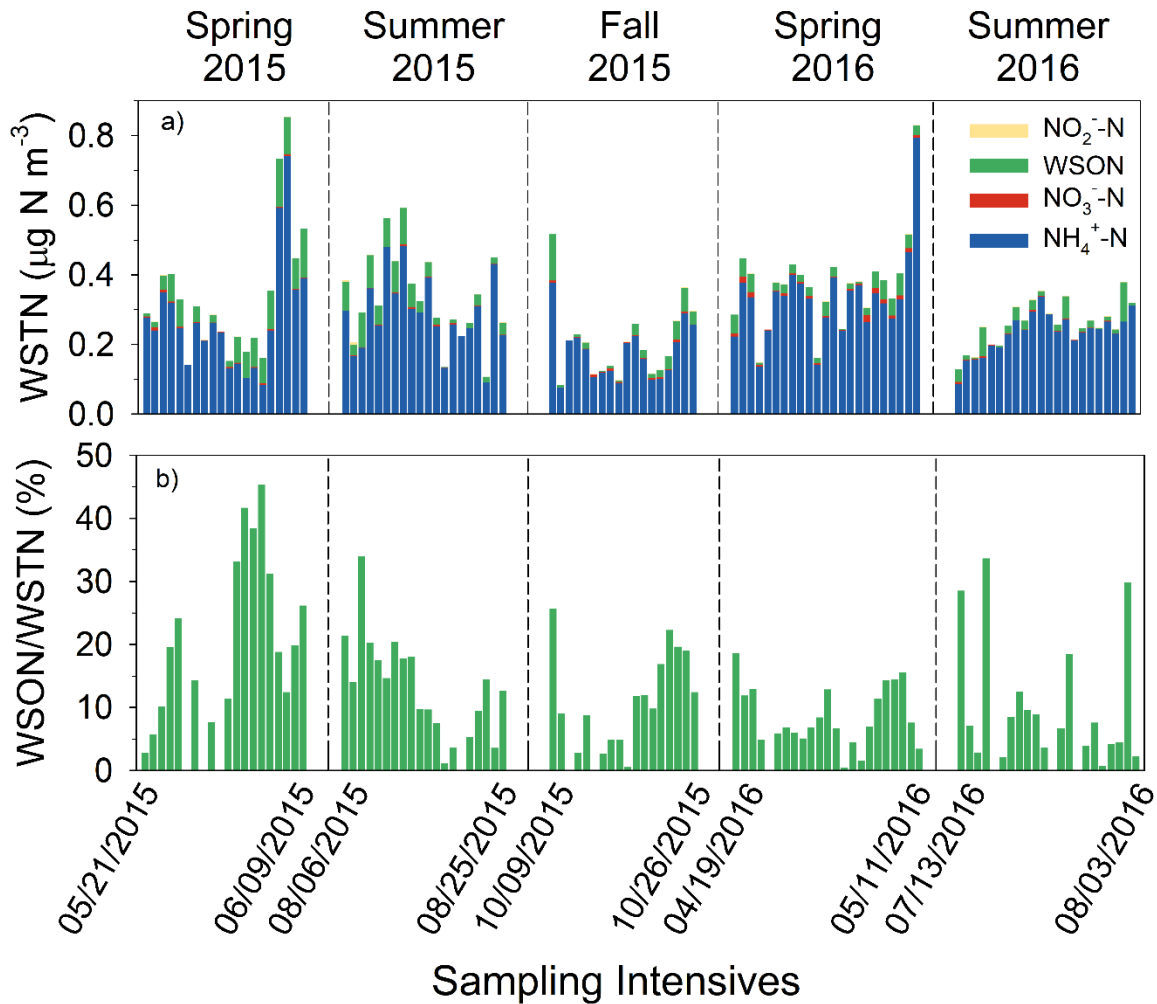
Figure 8. Contributions of N aerosol species to WSTN in 24-hour Hi-Vol $PM_{2.5}$ samples during seasonal SANDS intensives (a) along with percentage of WSON to WSTN (b).
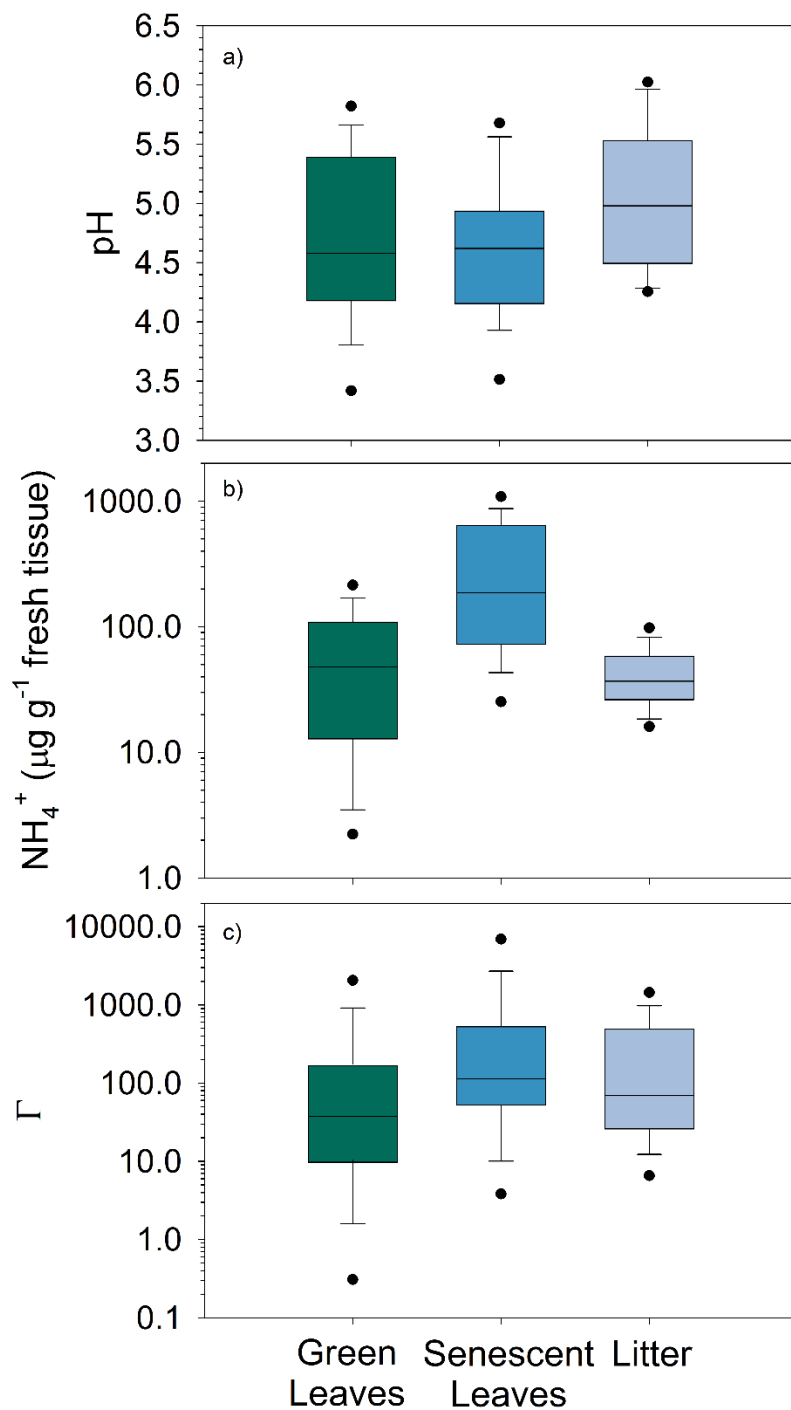
1230   Figure 9. Boxplots of pH (a), NH_4^+ (b) concentration (μg g^{-1} fresh tissue), and equivalent emission potential (Γ) (c) in tissue of green leaves, senescent leaves, and litter on the forest floor. Solid line inside box represents median. Top and bottom of box represent 75th and 25th percentiles. Whiskers represent 10th and 90th percentiles and dots represent 5th and 95th percentiles.
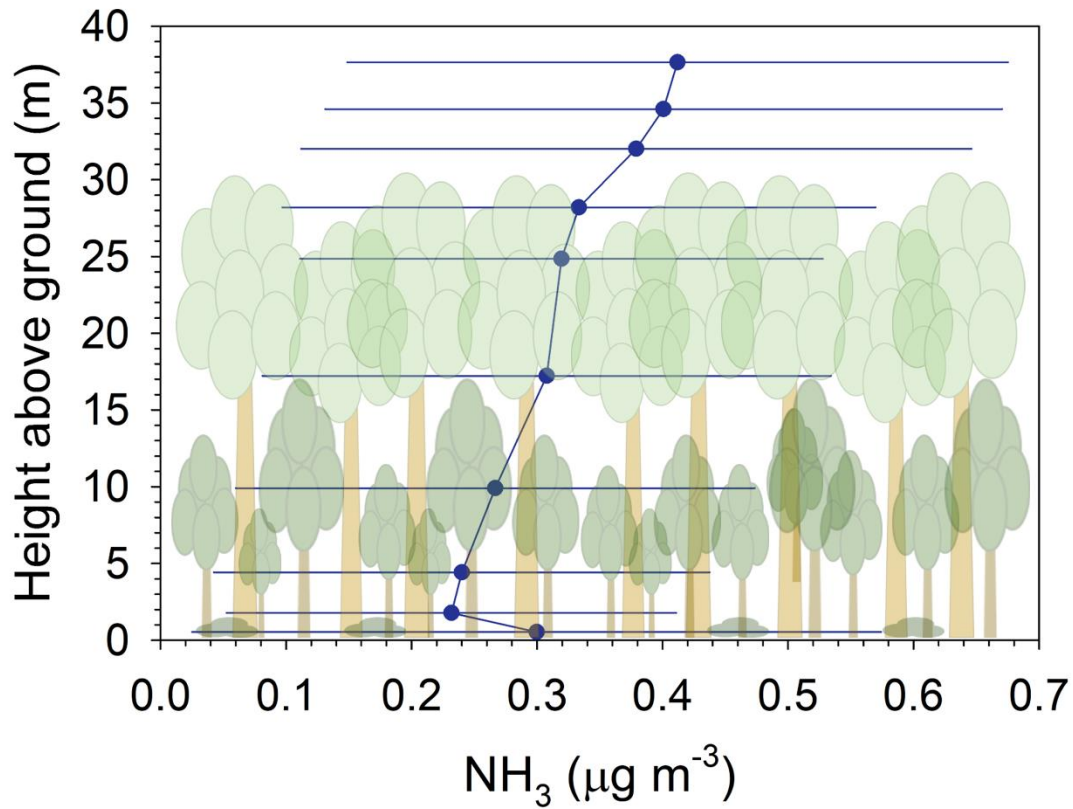
1235

Figure 10. Vertical concentration profiles of NH_3. Mean (filled circle) and standard deviation (bars) of concentrations are shown for $N = 76$ daytime profiles.
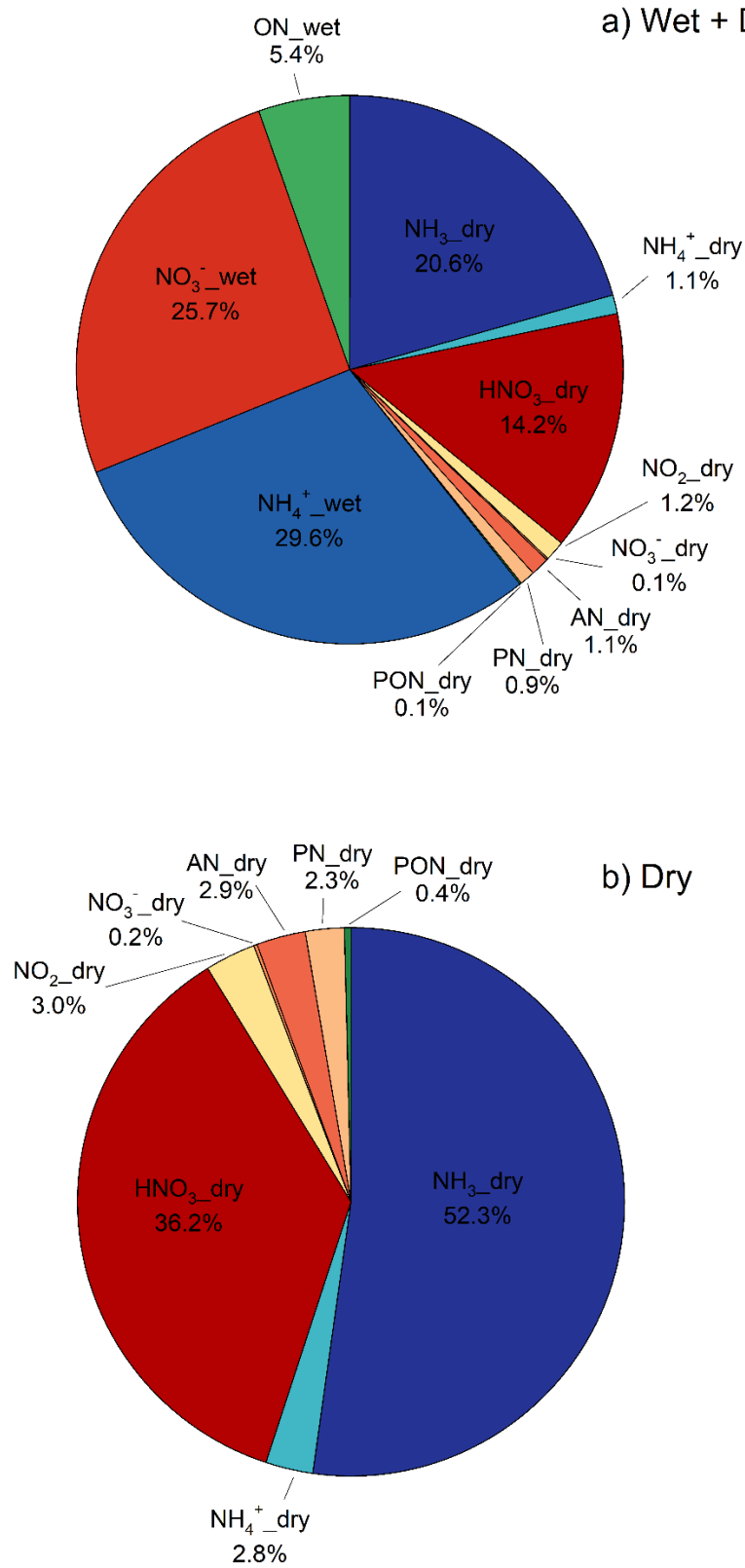
1240

Figure 11. Speciated annual total (wet and dry) (a) and dry (b) deposition showing percent contribution of individual components.
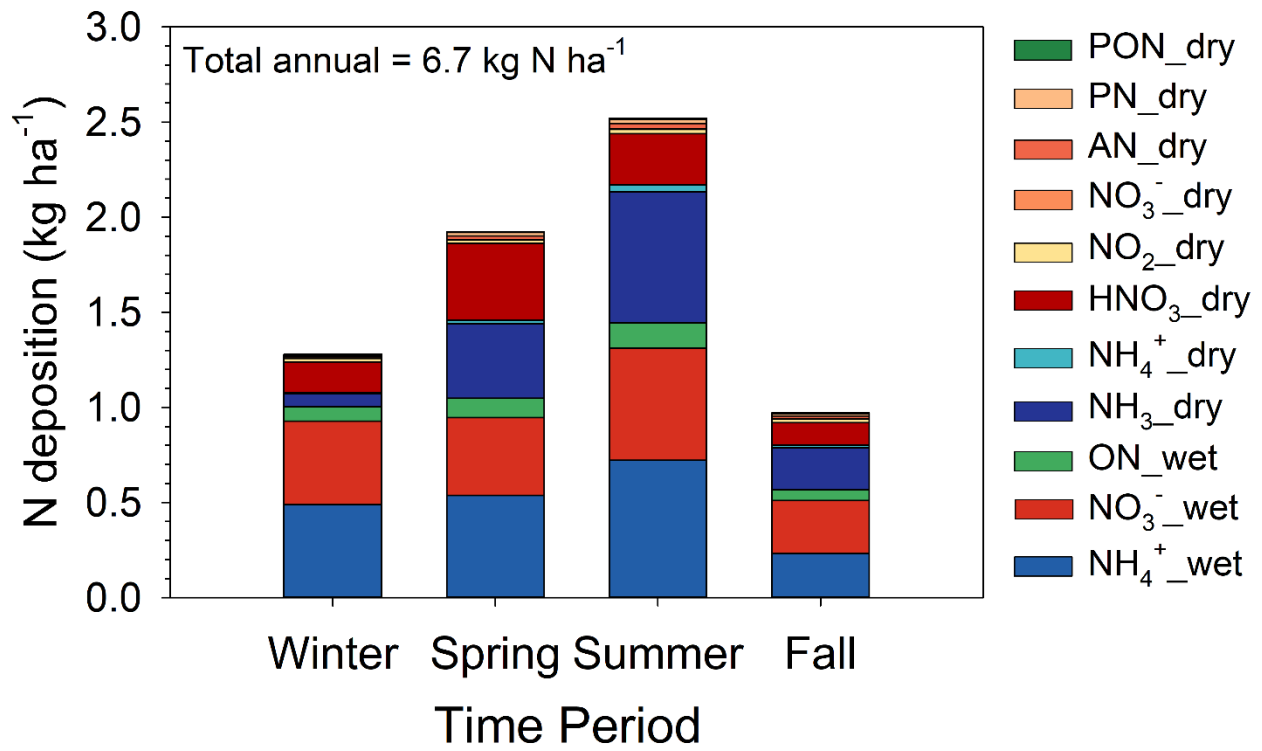
1245   Figure 12. Seasonal speciated deposition budget. Nr species are listed in the legend as defined in

the text, along with indication of the deposition pathway (dry or wet).
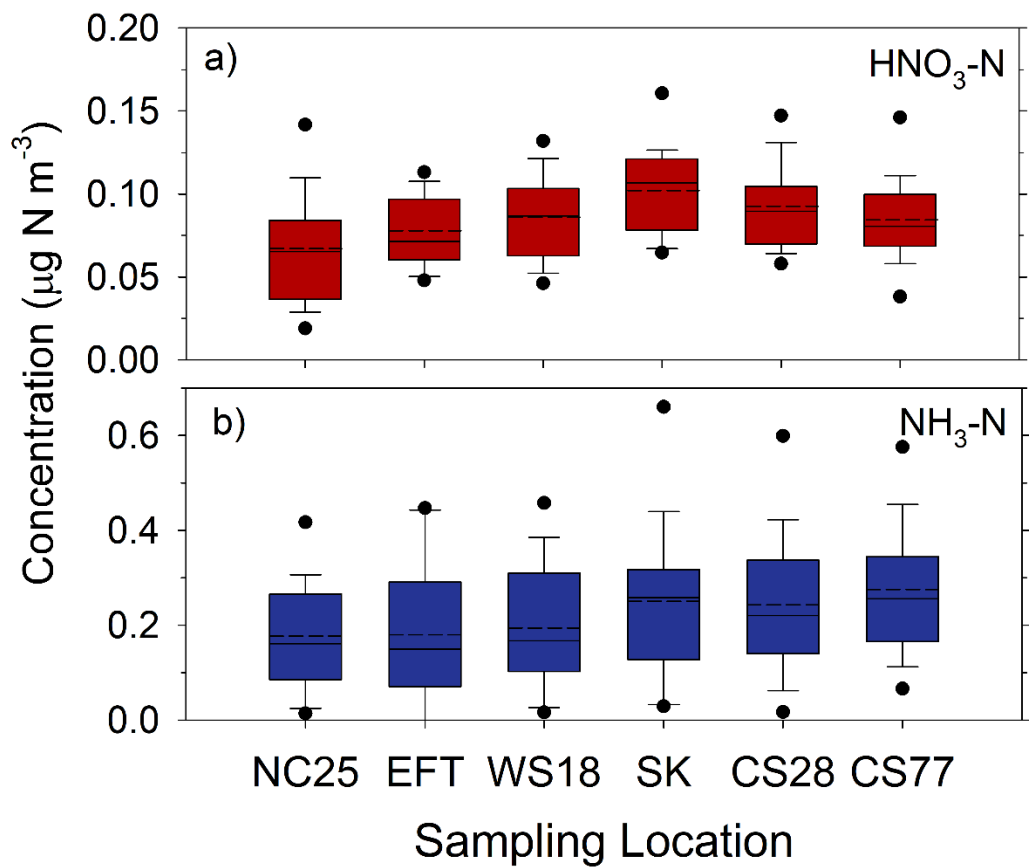
Figure 13. Concentrations (as N) of HNO_3 (a) and NH_3 (b) measured at different elevations, increasing from left to right (see Figure 1 and Table 1), across the Coweeta Basin. Solid and dash lines inside box represent median and mean, respectively. Top and bottom of box represent 75th and 25th percentiles. Whiskers represent 90th and 10th percentiles and dots represent 95th and 5th percentiles.